Theses, Dissertations and Culminating Projects

5-2015

On the 3-Dimensional Fluid-Structure Interaction of Flexible Fibers in a Flow

Ryan Howard Allaire

MONTCLAIR STATE UNIVERSITY

On the 3-Dimensional Fluid-Structure Interaction of Flexible Fibers in a Flow

by

Ryan H. Allaire

A Master's Thesis Submitted to the Faculty of

Montclair State University

In Partial Fulfillment of the Requirements

For the Degree of

Master of Science, Pure & Applied Mathematics Concentration

May 2015

College of Science and Mathematics

Thesis Committee:

Bogdan Nita

Department of Mathematical Sciences

Ashwin Vaidya

05/08/15

Date

Arup Mukherjee

On the 3-Dimensional Fluid-Structure Interaction of Flexible Fibers in a Flow

A THESIS

Submitted in partial fulfillment of the requirements

For the degree of Master of Science

by

Ryan Howard Allaire

Montclair State University

Montclair, NJ

2015

Abstract

We discuss the equilibrium configurations of a flexible fiber clamped to a spherical body and immersed in a flow of fluid moving with a speed ranging between 0 and $50cm/s$. Experimental results are presented with both two-dimensional and three-dimensional numerical simulations used to model this problem. We present the effects of flow speed and initial configuration angle between the fiber and the direction of the flow. Investigations reveal that both the orientation of the fiber and the fiber length have a significant impact on the deformation of the fiber as well as on the forces it experiences. Specifically, we measure the drag and lift experienced by the system and measure them against known values in literature. We note, additionally, that longer fibers (i) bend significantly more than shorter fibers and (ii) display oscillatory or flapping motion at much lower flow speeds than their shorter counterparts. In the two-dimensional simulations we reveal that the drag on the fiber is noticeably affected by the size of the sphere. The analysis of the drag is done in terms of Vogel exponents, computed in both 2-D and 3-D, and is compared with the literature. The validity of the reduction of dimensionality is tested against the three-dimensional simulations and qualitatively compared. Both mesh density and convergence studies are performed in 2-D and 3-D to balance the accuracy and convergence rates. We also discuss the robustness of the three-dimensional model and the practicalities of using a lower-dimensional model.

Acknowledgments

I would like to thank my friends and family for their love and support throughout the years. I am very grateful for my committee members, Drs. Bogdan Nita, Ashwin Vaidya, and Arup Mukherjee for their comments and constructive advice they have given over the past few years. I would like to especially thank Dr. Bogdan Nita for reaching out to me in my first year to start research. I am sincerely grateful for the continual mentorship in the Complex Fluids Laboratory by Dr. Ashwin Vaidya and for him making it feel like home.

Contents

iv

List of Figures

List of Tables

Chapter 1

Introduction

This paper focuses on the problem of equilibrium (re)configuration of deformable fibers in a flow. Other than the well known engineering applications of this problem, flexible fluid-structure interactions are ubiquitous in nature and their biological applications are particularly interesting. The problem of snoring, for instance, has its roots in a fluid-structure interaction, where the fluid is air and the structure corresponds to the soft-palette in the pharynx whose oscillations induce snoring[18]. A second widely studied application is the dynamics of ciliary hairs which line much of the human body and whose motion helps propel bodily fluids[27]. The breakdown of the ciliary mechanism is the cause of several human pathologies and constitutes an important medical question. Fluid structure problems are also essential to our understanding of the mechanics of flying and swimming[7]. The investigation of the positioning and orientation of wings, their length and equilibrium configurations, flapping modes, can all assist in optimal flight design. In the context of plant biology, the pioneering work by Vogel[33, 34] has lead to considerable attention to issues of forces experienced by plants in high winds[16, 23]. The flexibility of plants and aquatic vegetation can provide important clues of their health.

The fundamental phenomenon of the terminal state, including velocity and orien-

tation, of a rigid body in a fluid flow has been well studied for over a century. Despite the attention to this problem, several significant fundamental questions remain unanswered. In the past few decades, effort has been spent on explaining the terminal orientation of rigid symmetric bodies in a flow (where the structure is freefalling or hinged with one degree of rotational freedom) [5, 10, 11, 12, 20, 22, 26, 32, 37]. Our previous studies on hinged cylinders reveal that when the flow speed (or Reynolds number) is very low, the cylinder maintains its initial orientation. However as the Reynolds number exceeds a certain threshold, determined by the inertia in the system, the cylinder aligns with its longest axis perpendicular to the direction of the flow which is a new stable equilibrium. Beyond a second threshold for the Reynolds number, the particle begins to display complex unsteady behavior such as periodic oscillations and autorotation[5, 26, 24]. These varying orientations of a rigid body have a lot to do with the structure of the vortex shedding around the body. When the suspended body has the additional characteristic of being flexible, the physics becomes even more complicated. This thesis is a part of an ongoing contribution to the broader subject of terminal orientations and configurations in fluid-solid interaction and aims on extending previous work to flexible systems.

Many studies of fluid-structure interaction have been done in compressible fluids (air). The modeling of unmanned air vehicles (UAV) has a significant role in aerodynamics. The optimization design of aircraft stems in computation of drag coefficients. In our work we analyze drag coefficients for different configurations and geometries (2-D and 3-D). This study was computed for low Reynold's number. We expand upon this three-dimensional model to higher Reynold's numbers [6]. Additionally, studies have been done with medical applications. Numerical studies have been done to analyze the airflow in human vocal folds. Specifically, the modeling of the interaction between air and the vibrations made when one talks is used with potential application in planning of surgeries, and voice rehab. Understanding of such elastic structures

and their interaction with fluids can greatly advance the medical industry [17]. Our study in flexible fibers helps analyze such biological structures and even analyzes the necessity (or lack thereof) of a three-dimensional model. Other studies are concerned with applications of fluid-structure interaction in hemodynamics. Work performed by researchers at the Southwest Hospital in China have created a method for measuring instantaneous blood pressure and flow by designing and implanting a Fabry-Perot fiber sensor via intubation [38] Understanding the interactions of these fiber sensors with blood flow can help accurately predict real-time blood pressure and flow. Our study can help determine the optimum design of such bio-mechanical devices.

Studies have been done for the strict sake of fluid-structure interaction. Numerous studies have been done on the classic flow past a cylinder. Research done by the Department of Aerospace Engineering at University of Naples analyzes the vortex structures formed behind finite and infinite cylinders in fluid flow. According to their work, for finite free-end cylinders the flexible fiber creates vortices that interact with the fixed end in a complex manner. Attribution is made to three-dimensional features of the flow for this complex behavior [13]. Our study specifically analyzes this complex behavior of flexible three-dimensional fibers, except that we are primarily concerned with flexible fibers clamped to a sphere. On a similar note, other studies have analyzed the flow around a sphere. Work done by engineers at MIT have analyzed the flow structure past a finite porous obstruction (sphere) in a channel [40]. The applications of obstructions range from aquatic vegetation to habitat for animals. If we understand the flow behind such objects, we can understand the complex evolution of these biological organisms. Porous objects improve water quality by blocking harmful materials. Our study generalizes this to obstructions with flexible fibers (similar to grass) and has similar applications. Significant work has been done on the analysis of drag coefficients on a sphere [6]. We quantitatively compare our results against these theoretical drag curves.

In a series of fundamental experimental and theoretical papers on a similar subject[1, 14, 29, 39] and others, it has been pointed out that deformable bodies in a flow bend in order to reduce drag. Alben et al.[1, 2] considered their study in a two dimensional soap film with flow velocities ranging between 0-3m/s. Along with their accompanying theoretical analysis, they predicted the scaling law for drag on flexible bodies, namely $F_D \propto U^{\frac{4}{3}}$. Gosselin et al.[14] have examined the reconfiguration of rectangular plates and circular disks in air flow for speeds up to 25m/s. Their theoretical analysis of the subject confirms previous findings but has also revealed important phenomena about deviation in deformation trends at large flow speeds observed by deviations in their drag scaling law. This thesis considers a flexible fiber submerged in a three dimensional flow in a water tank with speeds 0-50cm/s and is also concerned with some other, yet unexplored, aspects of the problem such as the effect of fiber length and orientation(θ_0). Unlike previous work, our study also considers the bending of the fiber in the presence of a basal body, which is taken here to be spherical. A basal body is naturally present in all physical examples and therefore accounting for it is essential.

The rest of the thesis is organized as follows. In chapter 2, we describe our experimental investigations, including the procedure and outcomes. Chapter 3 details our two-dimensional numerical simulations performed using the software Comsol Multiphysics. Chapter 4, on the other hand, details the three-dimensional numerical simulations based on the experiments. The details of the numerical schemes, convergence studies, and comparisons with experiments are presented.

Chapter 2

Experiments

Detailed experiments were conducted in this study on the interaction of a suspended, clamped fiber in a flow as a function of the fiber length, initial orientation(θ_0) and flow speed (U). The experiments were performed in a flow tank with recirculating water with flow velocities ranging between 0-50cm/s ($0 < Re = \frac{\rho_f U L}{\nu} < 30,000$ where ρ_f is the density of the fiber, U is the free stream velocity measured at the center of the tank in the absence of an obstacle and L is the fiber length). Fibers chosen for our study were made of nylon and polyester and were extracted from paint brushes. The exposed portion of the fibers were of lengths 2cm, 4cm and 6cm. These were inserted into a styrofoam ball of diameter 3cm in such a way as to prevent any motion with respect to the ball (Figure 2.1). The styrofoam ball with the fiber was held in place by means of a copper wire of thickness 1mm passing through the ball which was placed at the center of the tank appropriately to prevent any transverse or rotational motion. Panels (a) and (b) in Figure 2.1 show a side and back view of the fiber with the spherical basal body to which it is attached.
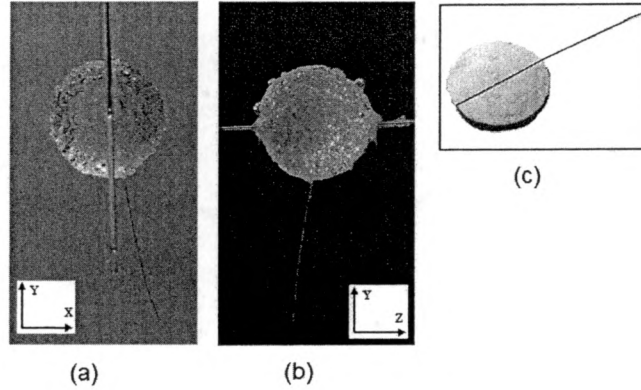
Figure 2.1: Experimental setup: panel (a) shows a side view of the fiber attached to the spherical body (b) shows a rear view of the same object and panel (c) shows the nylon fiber inserted into the styrofoam ball which serves as the basal body. The flow direction in the experiments occurs from left to right in panel (a) or out of the plane of the paper in panel (b)

The dynamics of the fiber in the flow were recorded using a digital camera (Sony α), placed orthogonal to the flow. The orientation of the fiber with respect to the flow were changed by appropriately rotating the styrofoam ball upon the copper wire before clamping it. In this study three different angles were considered (where angles are measured using the standard convention with respect to the horizontal axis, counterclockwise.), namely[1] 225°, 270° and 315°.

The results of our experiments study are shown in Figure 2.2. The primary experimental observation relates the bending of the various fibers as a function of the Cauchy number (Ca), which defines the ratio of inertial to elastic forces in the system. We define this number as $Ca = \frac{\rho U^2}{K}$ where ρ is the density of the fluid, U is the characteristic velocity and K is the bulk modulus of the fiber, which is taken to be $4 GPa$ in our experiments, corresponding to Nylon.

---

[1]In our numerical simulations for the problem, presented in the following section, the fibers were placed at the antipodal end of the spheres, i.e. at angles 135°, 90° and 45°. Due to the symmetry of the problem and absence of any gravitational effects on the fiber, these angles are similar to those used in experiments. However, henceforth in this text we will use the experimental angles when referring to the fiber orientation.
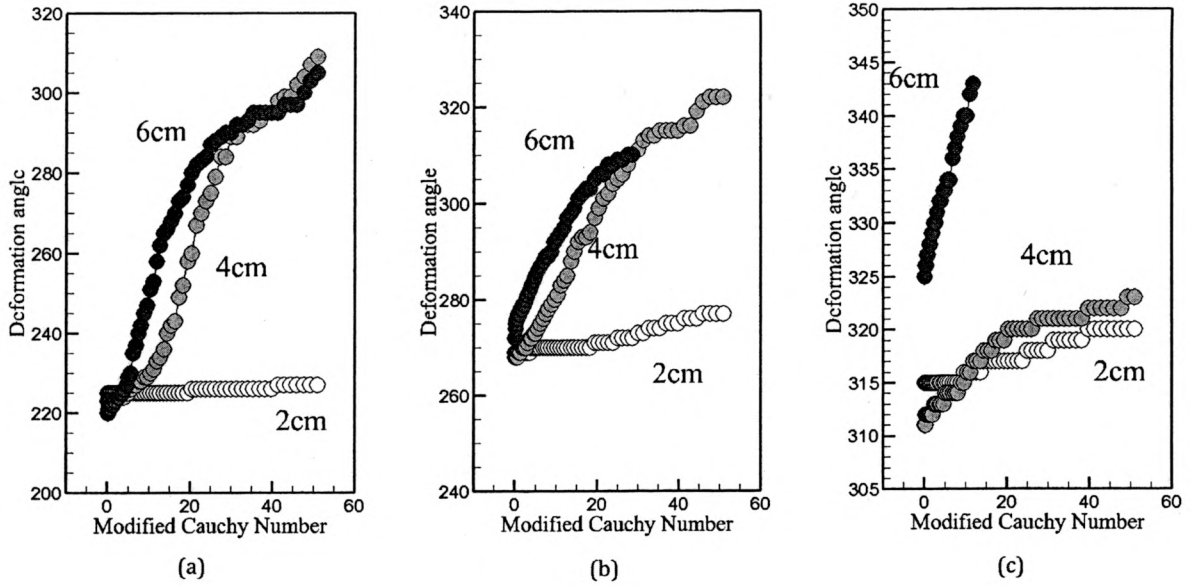
Figure 2.2: These graphs show the average bending of the fibers between their suspension point and free end based on experimental investigations. Variations of the bending with $\tilde{C}a$, fiber length and initial orientation are examined. Panel (a) corresponds to $\theta_0 = 225°$, (b) to $\theta_0 = 270°$ and (c) to $\theta_0 = 315°$.

Gosselin et al.[14] note that the drag on a flexible rectangular plate can be seen to depend on an appropriate scaling of Ca, defined by $\tilde{C}a = C_D \cdot Ca$ (where C_D is the drag coefficient) such that for $1 < \tilde{C}a < 10$ the flexible plate transitions to a reconfigured state.

Due to the difficulty in obtaining drag coefficients and flexural rigidity in our study, we use a simple rescaling of the Cauchy number, $\tilde{C}a = 10^{-12} \times Ca$ to bring it to the same scale as in previous studies.

Figure 2.2 shows the average bending of the fibers as a function of $\tilde{C}a$ for various dimensions of the fiber and different initial configurations. The average bending is estimated by the angle of the straight line connecting the points P and Q where P is the point on the fiber in contact with the ball and Q is the free end of the fiber. The bending is shown for the three fibers of different lengths as well as the initial orientation angle of the fiber(θ_0). Increasing $\tilde{C}a$ has the effect of greater bending

force upon the fiber. Our observations reveal that beyond a certain critical value of $\tilde{C}a$, which depends upon the material of the fiber and its physical dimensions such as length and thickness, the fiber begins to bend and continues to do so until it reaches a second critical $\tilde{C}a$, which we shall refer to as $\tilde{C}a_c^{(2)}$, when it starts to display time dependent motion. Since the focus of this paper is the equilibrium configuration of the fiber, the $\tilde{C}a$ was restricted to the range below $\tilde{C}a_c^{(2)}$. The longer fibers display greater propensity to bending, and eventually flapping or random motion, than the shorter ones and start to bend for smaller values of $\tilde{C}a$ as seen from the slopes of the tangents to these curves; the 2cm fiber shows a minimal change with respect to its initial configuration.

The average bending is seen to be highest when the fiber protrudes more into the incoming flow ($\theta_0 = 225°$) and least for the case of $\theta = 315°$ where the fiber is closer to the wake region making the body more streamlined. We can use the changes in concavity of the deformation angle data to identify the values of $\tilde{C}a_c$. The value of $\tilde{C}a_c$ is seen to depend on the fiber length as well as the orientation. For the case $\theta_0 = 225°$, $\tilde{C}a_c$ is of $O(1)$ for the 6cm fiber and shifts to $O(10)$ for the 2cm and 4cm cases. For the remaining angles the 6cm fiber displays no yield stress while $\tilde{C}a_c$ for the 4cm and 2cm fibers show an order of magnitude reduction. The shorter fibers in the experiments, namely 2cm and 4cm, display time dependent fluttering at the highest velocity considered here but the 6cm fiber achieves the time dependent flapping at much lower values of $\tilde{C}a_c^{(2)}$ than the other cases. It must be however noted that unsteady motion referred to here was not the consistent large periodic oscillation of the type observed by [28].

Visualizations of the flow structure past the body indicates a complex wake vortex pattern even at fairly low velocities(figure 2.3). The resulting pressure differences
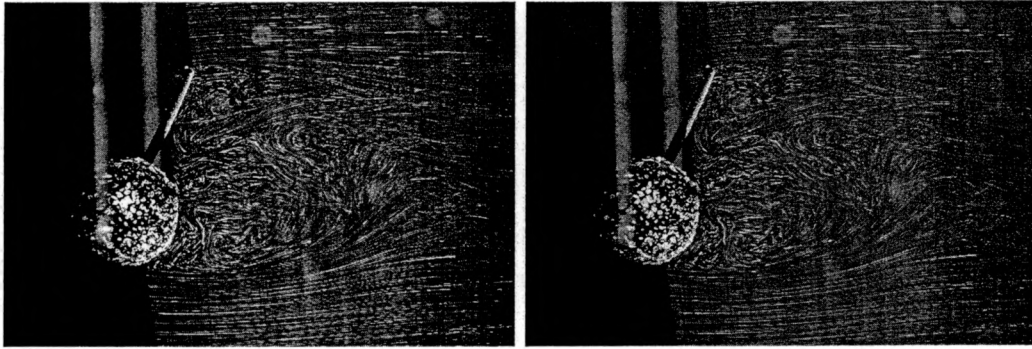
Figure 2.3: Visualization of the wake vortex behind the fiber. Panel (a) shows the vortex structure for a $4cm$ fiber at approximately $U = 5cm/s$ while panel (b) shows the structure for a $6cm$ fiber at a higher velocity of $U = 15cm/s$.

between the fore and aft regions of the fiber eventually cause the bending of the fiber as the pressure force exceeds the tension in the fiber. To allow for the visualization past the fiber, we repeated the aforementioned experiments with a thicker fiber. The flow was seeded with microscopic hollow glass spheres of average diameter $13\mu m$ and illuminated using a laser sheet (532nm, 1W laser from Opto Engine LLC). The resulting images of the flow structure via scattering from the seeded particles are shown in figure 2.3.

Visualization of the flow structure along the YZ plane was also conducted in order to discern any significant three dimensional effects. The spherical basal body generates a noticeable dimensional wake; the fiber is however, far too thin to do so. The figure 3.7 depicts the three dimensional flow structure in the plane Z and it shot from an oblique angle to allow for visual identification of the flow structure. The fiber used for purposes of visualization are thicker (3mm width) than the nylon fibers referred to earlier since the flow past the nylon fibers are practically impossible to visualize due to their slenderness. The red box in figure 3.7 highlights the three dimensional structure which can be seen to be obvious behind the sphere but not as prominent behind the fiber and remains sufficiently small for the flow speeds examined in this study.

Also, it is reasonable to assume that the symmetry of the flow around the fiber cancels any bending forces along the YZ plane; the flow asymmetry in the XY plane, along which the fiber lies is the only cause of the bending which occurs in the same plane. As a consequence of these observations our following analysis are conducted in two dimensions. Also, while we were unable to measure the drag and lift forces experimentally, they have been studied numerically and discussed in the following section. Close comparisons with experimentally observable parameters are also made to estimate deviations of theoretical results from experiments. Furthermore, the three dimensional computation remains a considerable challenge at this stage in terms of its computational cost and time.

Chapter 3

2-Dimensional Numerical Simulations

We performed a two dimensional numerical simulation for the problem using the software Comsol by employing the Fluid Structure Interaction (FSI) module.

3.1 The governing equations and numerical scheme

The resolution of this fluid-structure problem followed from solving the following coupled equations:

$$\rho_f \left(\frac{\partial \mathbf{u}}{\partial t} + \mathbf{u} \cdot \nabla \mathbf{u} \right) - \mu \nabla \cdot (\nabla \mathbf{u} + \nabla^T \mathbf{u}) + \nabla p \ = \ \mathbf{f} \tag{3.1}$$

$$\nabla \cdot \mathbf{u} \ = \ 0 \tag{3.2}$$

$$\rho_s \frac{\partial^2 \mathbf{u}_s}{\partial t^2} - \nabla \cdot \sigma \ = \ \mathbf{F}_v \tag{3.3}$$

where $\mathbf{u}$ is the incompressible fluid velocity field, $\mathbf{u}_s$ is the displacement of the solid fiber, t is time, ρ_f is the density of the fluid, ρ_s is the density of the solid, μ is the dynamic viscosity, $\mathbf{f}$ is the external volume force on the fluid and $\mathbf{F}_v$ is the force per unit volume on the fiber. At the channel inlet, the flow is taken to be fully developed

and parabolic while at the chancel outlet, zero pressure conditions are imposed. The
Cauchy stress tensor for the solid material, σ, is given by[30]

$$\sigma \quad = \quad \frac{1}{det(\mathbf{F})} \mathbf{F} \mathbf{S} \mathbf{F}^T \tag{3.4}$$

where $\mathbf{F} = (\mathbf{I} + \nabla \mathbf{u}_s)$, $\mathbf{S} = \mathbf{S_0} + \mathbf{C} : (\epsilon - \epsilon_0)$ and $\epsilon = \frac{1}{2} \left(\nabla \mathbf{u}_s + \nabla \mathbf{u}_s^T \right)$. Here $\mathbf{C}$, $\mathbf{S}$,
$\mathbf{S_0}$, ϵ and ϵ_0 stand for the stiffness tensor, stress tensor, initial stress tensor, strain
tensor and initial strain tensor, respectively. In the special case of a homogeneous
isotropic media, like considered in our study, σ reduces to the simple form

$$\sigma_{ij} \quad = \quad K\delta_{ij}\epsilon_{kk} + 2\mu_s \left(\epsilon_{ij} - \frac{1}{3}\delta_{ij}\epsilon_{kk} \right) \tag{3.5}$$

where K is the bulk modulus and μ_s is the shear modulus of the material.

On the solid boundaries of the channel, no-slip conditions are imposed. On the
deformable body, the flow velocities are taken to be equal to the rate of deformation
of the fiber (i.e. the time rate of change of the displacement).

The FSI module solves the Navier-Stokes equations for the flow in a continuously
deforming geometry using the *arbitrary Lagrangian-Eulerian* (ALE) technique. The
deformation of the mesh relative to the initial shape of the domain was computed using
hyperelastic smoothing. Inside the fiber, the moving mesh follows the deformations of
the fiber and at the exterior boundaries of the flow domain the deformation was set
to zero in all directions. A *fine* mesh was chosen specifically to be calibrated for fluid
dynamics problems (see figure 3.3). We solved for the time dependent variables using
the PARDISO solver (included in Comsol) which was run for 5 seconds in increments
of 0.5 seconds. Once the flow field was computed, we also evaluated the net drag and

12

lift forces on the fibers as a function of the flow velocity:

$$F_D = \mathbf{U} \cdot \oint_S \mathbf{T} \cdot \mathbf{n} \, dS, \qquad F_L = \oint_S p \, \mathbf{k} \cdot \mathbf{n} \, dS, \tag{3.6}$$

where S is the surface of the obstacle, $\mathbf{T}$ is the Newtonian stress tensor, p refers to the pressure, $\mathbf{n}$ is the normal unit vector pointing into the body and $\mathbf{k}$ is the unit vector normal to the direction of the free stream. Parameters used for the study are shown in table 6.1.

3.2 Convergence tests

Several tests were performed to confirm the validity of our computational results. In particular, we investigated the effect of mesh density by computing the steady state drag and lift forces for various mesh density options, as shown in figure 3.1. The x axis denotes the various mesh configurations, where 1 is defined as a 'custom mesh'(11381 elements) , 2 as 'coarser'(2212 elements), 3 as 'coarse'(3590 elements), 4 as 'normal'(5241 elements), 5 as 'fine'(8609 elements), 6 as 'finer'(16768 elements), 7 as 'extra fine'(37456 elements) and 8 as 'extremely fine'(66682 elements). Numerical convergence was achieved (figure 3.1) and the result seem stable beyond the choice of *normal* mesh. Mesh 1 was user controlled while meshes 2-8 were automatically generated by Comsol. Based on these estimates we chose the 'fine mesh' or higher to run all our cases, with grid points ranging between about 9000-12000.
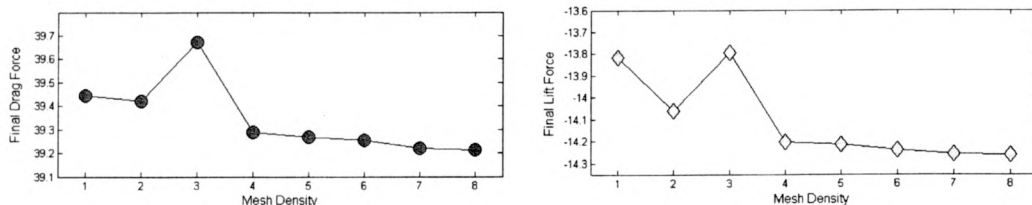
13

Figure 3.1: The values for drag and lift are computed for a 4cm fiber of thickness 0.05cm with initial orientation $\theta_0 = 270°$ relative to the flow, as a function of different mesh densities. Here the x axis denotes the various mesh configurations, where 1 is defined as a custom mesh, 2 as 'coarser', 3 as 'coarse', 4 as 'normal', 5 as 'fine', 6 as 'finer', 7 as 'extra fine' and 8 as 'extremely fine'.
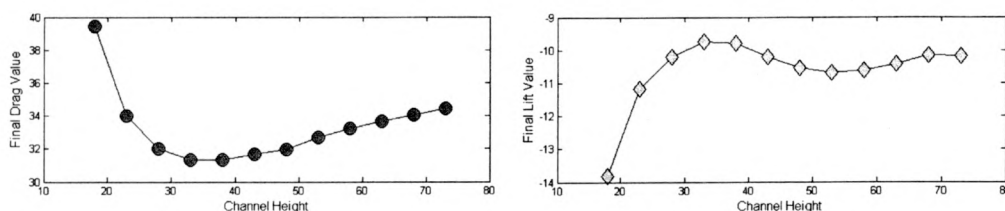
Figure 3.2: The values for drag and lift are computed for a 4cm fiber with initial orientation $\theta_0 = 270°$ relative to the flow, as a function of different channel heights.

Our computational domain was chosen to match with experimental configuration, apart from the restriction in dimensionality. For this reason the majority of the computational results reported here correspond to the case of $h = 18$cm. Variations in the values of terminal drag and lift forces for increasing channel heights(in centimeters) were computed and are depicted in figure 3.2 for the sample case of a 4cm fiber at initial angle $\theta = 270°$. Increasing channel heights naturally changes the drag and lift forces which appear to converge to a fixed value. There is a change of nearly 20% in the drag force and about 25% in the lift force as one moves from $h = 18$cm to the final channel height of $h = 75$cm considered here. It needs to be kept in mind that the convergence of the computed quantities with respect to h is not in question here; the choice of h is dictated by experimental considerations.
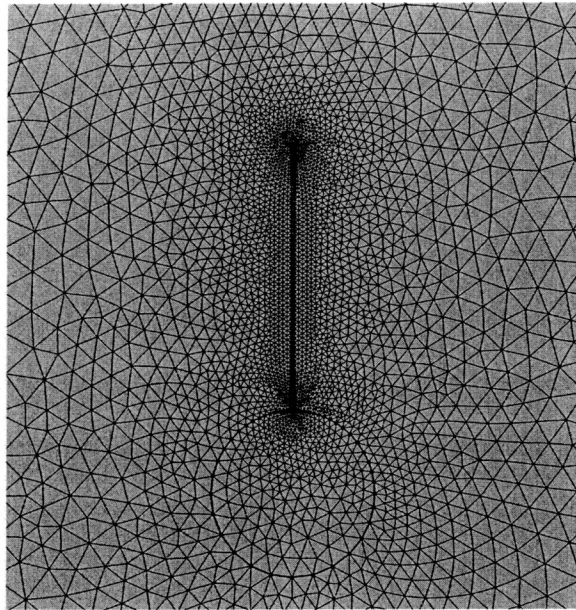
Figure 3.3: The two-dimensional triangular *fine* mesh generated in Comsol for the fluid structure problem under investigation.

3.3   Results: comparison with experiments

At the conclusion of the experimental section above we presented our flow visualization data indicating negligible three dimensional flow around the fiber. This is not to say that there is no three dimensional flow behind the fiber or that the fiber remains unaffected by the flow induced by the basal body. We use these observations to restrict our initial computational investigations to two dimensions. The three dimensional simulation is extremely challenging and will be pursued in our future work. In this section we discuss the relative merit of the numerical method employed to simulate and qualitatively replicate the experimental results. We do so by comparing the numerical estimates of the average bending versus $\tilde{C}a$ with those obtained from experiments (see figure 2.2).

A time sequence of the results of our simulations are shown in figure 3.5 for the same cases explored in experiments. The simulations permit us to visualize the evo-

lution of the two dimensional vortex structures and its interaction with the bending of the fiber. As anticipated, the wake structure and resulting pressure differential in the fore and aft regions of the fiber appears to be the driving factor causing the fiber to reconfigure. While the fiber orients into the flow, the primary cause of the first vortex is the fiber. In the streamlined position, it is the sphere which affects the primary vortex (see also figure 2.3) the most while with the fiber in the vertical orientation, the ball and fiber, both contribute equally to the primary vortex.
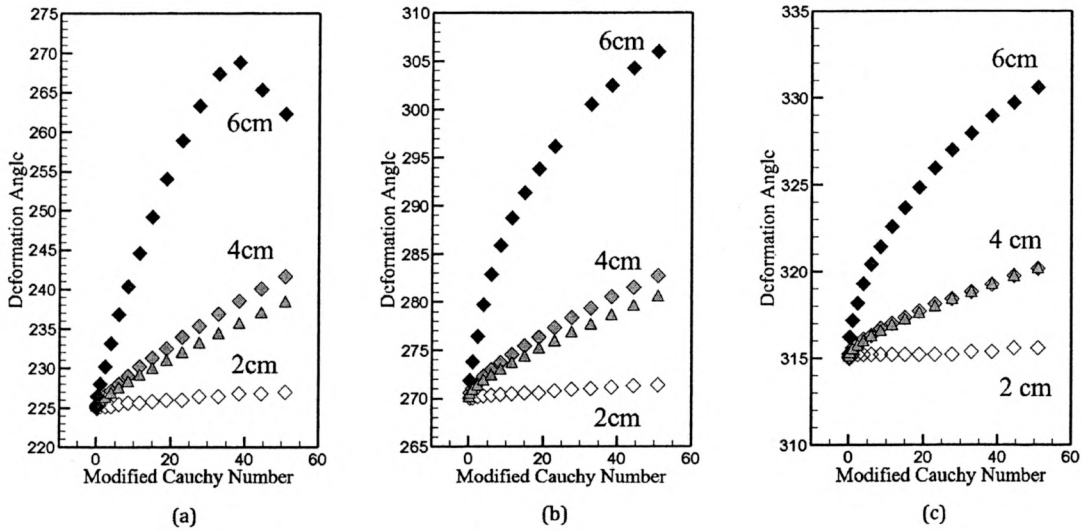
Figure 3.4: These graphs show the average bending of the fibers, between their suspension point and free end, versus $\tilde{C}_a$ for three different fiber lengths and initial orientations, based on the 2d numerical simulations. Panel (a) corresponds to $\theta_0 = 225°$,(b) to $\theta_0 = 270°$, and (c) to $\theta_0 = 315°$.

Figure 3.4 examines the average bending behavior versus $\tilde{C}a$ where the same range in $\tilde{C}a$ has been maintained as in experiments. The numerical results are in good qualitative agreement with experiments and show the same overall profiles observed in figure 2.2. Specifically, we note that the average deformation angle increases sharply with the length of the fiber, i.e. longer fibers are more prone to bending than the shorter ones. The 2cm fiber displays little propensity to bend, much like in ex-

16

Figure 3.5: The time evolution of a $4cm$ fiber at various orientations are depicted along with the corresponding flow structure. The fibers achieve their steady configurations as the flow simultaneously evolves into its steady state. The wake vortex structure is also seen to depend on the fiber orientation.
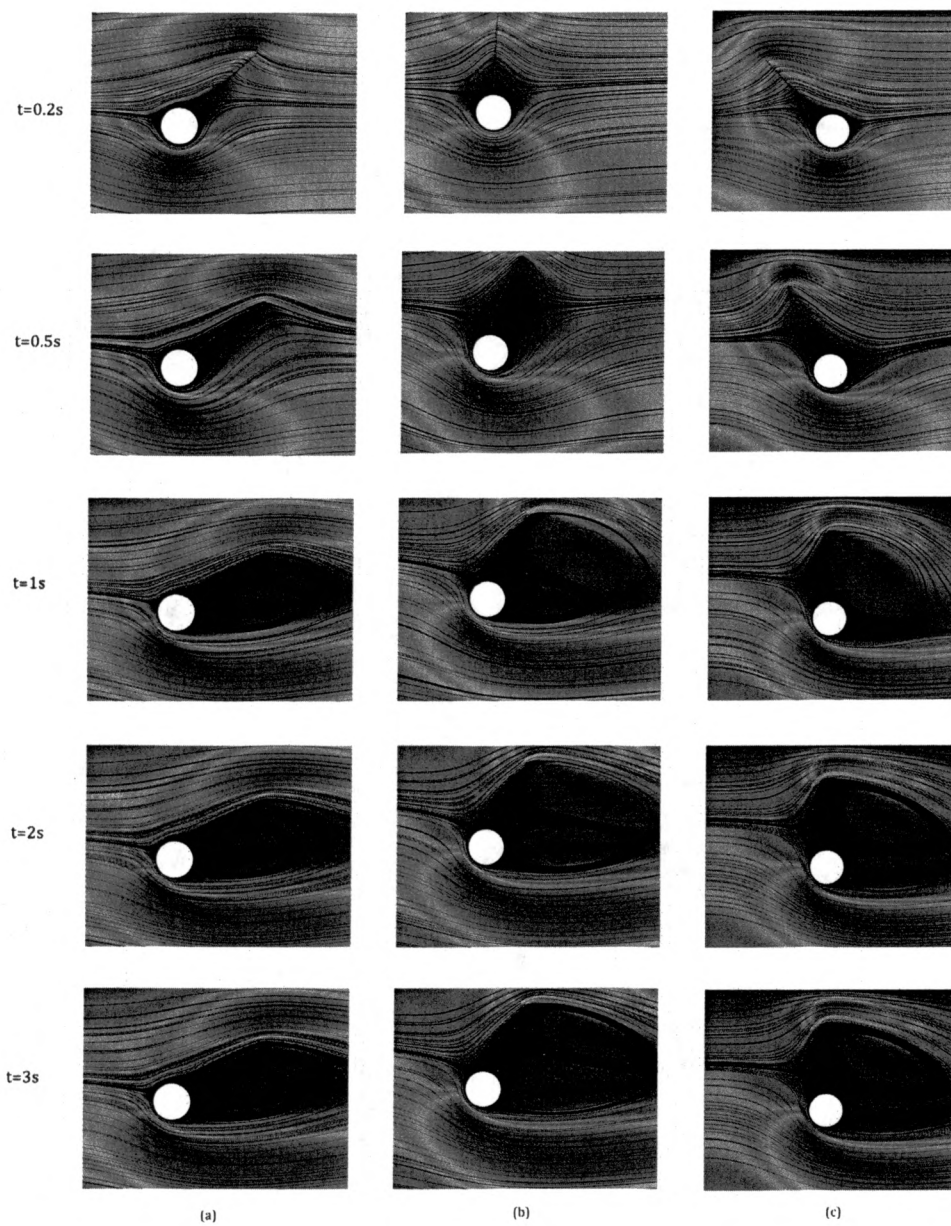
periments. In terms of orientation, the deformation angle is largest when the fiber protrudes into the flow direction and least when the fiber is in a more streamlined configuration (see also figure 3.6(d)). This is not so obvious for the 6cm fiber which shows a drop in the average bending past $\tilde{C}a \approx 40$ which is caused by the free tip of the fiber dropping below its maximum height in this orientation. While the 4cm and 6cm fibers show no critical behavior (i.e. absence of $\tilde{C}a_c$), the 2cm fiber exhibits critical behavior at $O(10)$ for the streamlined case and at $O(1)$ for the remaining two orientations. In these cases, the deviations from experimental observations can be attributed primarily to the mismatch of material properties of the fibers which had to be approximated in experiments. We also considered the case when the diameter of the basal body is reduced from 2.5cm to 0.06cm (note the triangular points in figure 3.4), in order to understand the impact of the body size on the fiber deformation. Our preliminary calculations revealed that the diameter of the basal body does indeed make a noticeable difference when the fiber protrudes into the flow but is less so when the fiber is in a streamlined position.
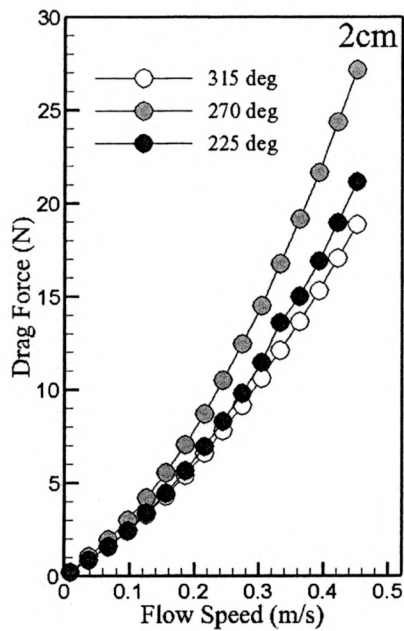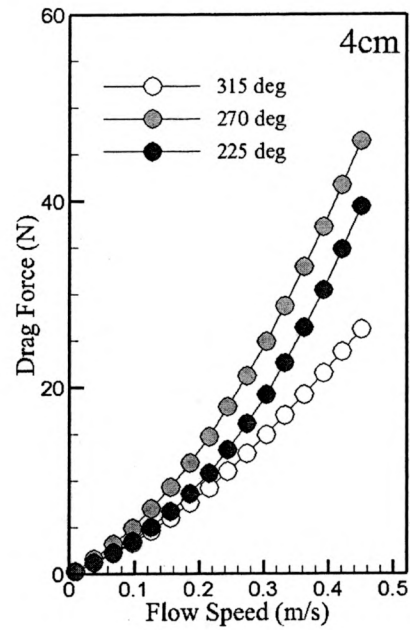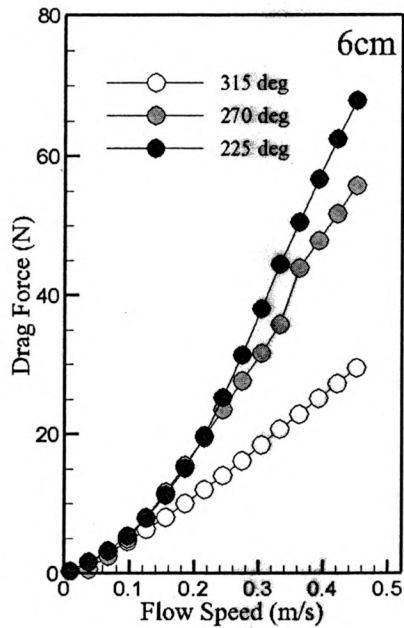
Figure 3.6: The panels (a)-(c) show variations in drag versus U. Panel (d) shows the drag transition of a sample case, the 4cm fiber at $\theta_0 = 270°$. In all cases here, the fiber is seen to reach steady state at about 1s with the highest drag when the fiber protrudes into the flow and the least drag when the fiber is in its most streamlined configuration.
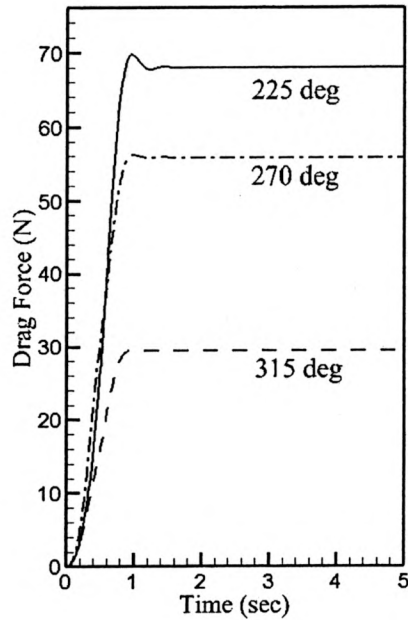
19

The x-axis in figure 3.4 was chosen to conform with the experimental range. In this range, no time dependent motion was observed for any of the fibers. However, we extended our study to explore values of $\tilde{C}a_c^{(2)}$ for the 2cm and 4cm fibers(the 6cm fibers broke down in the unsteady regime), each oriented at three different configurations. These simulations also display sensitivity to the orientation of the fiber. At certain critical flow speeds the fibers transition from steady state

Critical Speeds	225°	270°	315°
2cm	75.08 cm/s	42.63 cm/s	305.18 cm/s
4cm	39.68 cm/s	54.43 cm/s	83.93 cm/s

Table 3.1: Critical flow speeds at which the fibers display periodic oscillations.

to periodic oscillations, which are not actually observed in our experiments, in the range of flow speeds considered. Table 3.1 denotes the critical speeds which triggers the onset of oscillations. As in experiments, the larger fibers transition out of equilibrium more easily than the smaller ones. However, unlike in experiments, the simulations indicate that fibers oriented at $\theta_0 = 225°$ oscillate at lower flow speeds than the $\theta_0 = 315°$. This apparent discrepancy can be attributed to lack of a sufficient range of speeds in the observations, non-constant stiffness across the fiber and possibly, three-dimensional effects.

Drag Exponent	315°	270°	225°
2cm	1.19	1.24	1.22
4cm	1.19	1.26	1.29
6cm	1.14	1.28	1.40
4cm (small sphere)	1.20	1.33	1.30

Table 3.2: The drag exponents for fibers of varying lengths and orientations based on least squares fit of our 2D simulations.

Yet another way to classify the effect of the flow upon the bending configurations

of the fiber is by examining the overall drag on the system. It is well known that for rigid bodies the drag force varies as the square of the velocity[4]. However for flexible bodies, since the bodies can bend to reduce drag, the relation is markedly different from the rigid body case and can be given by $F_D \propto U^\alpha$ [34] where, the exponent, $1 < \alpha < 2$. Several studies performed on flexible bodies of different shapes and materials seem to put the exponent in the range 1-1.5 [1, 14, 34]. It is to be noted that in these studies the body is always initially held perpendicular to the flow direction. The results of our calculation of the drag exponent are indicated in the table 3.2. A least squares fit to the drag force values applied to the results of our two dimensional numerical computations (see figure 3.6) yield the values of α which seem to conform to the previously reported ranges. The exponents are seen to be sensitive to the orientation and length of the fiber although it is not quite clear if there is any distinct pattern. It has been observed [14] that there is a critical length below which the drag shows an increasing trend and above which the drag decreases with increasing length. While no such trend is seen here, it is plausible that such a reversal also shows itself as we combine the fiber length with its orientation. The values obtained in our computations clearly correspond to the case of small deformations [14, Table 1]; after all the velocities considered in our study are well below $1ms^{-1}$.
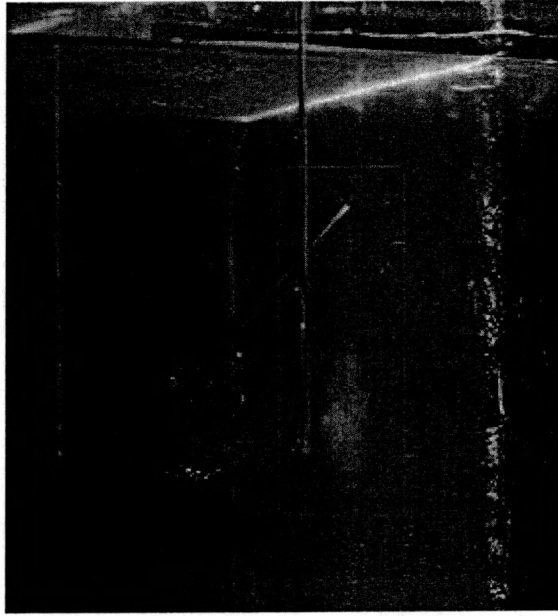
Figure 3.7: The image shows the wake vortex behind the obstacle in the Z direction. The fiber used here is $6cm$ in length and the corresponding flow velocity is nearly $15cm/s$. The picture in the red box shows the three dimensionality of the wake flow field. The fuzzy circular region behind the sphere corresponds to the 3-D wake structure behind the sphere; the fiber, however, does not generate any noticeable wake in the third dimension.

Chapter 4

3-Dimensional Numerical Simulations

In this section, 3-dimensional simulations are used to better portray the experiments described in Chapter 1. The differences between two and three dimensions, specifically the numerical calculations, will be discussed in detail. In this Chapter we describe the differences in assembly, solver configurations, and accuracy of solutions in reference to the modeling of the experiment.

4.1 Equations and Conditions

Navier-Stokes and Linear elasticity Equations (3.1),(3.2),(3.3) are again used to model the structural deformation of flexible fibers. In the 3-dimensional model we model the steady-state solution of the problem, since we are strictly concerned with the steady drag force and final bending angle. This fluid-structure interaction model is known as a two-way boundary coupling, in that the structural deformation affects the fluid flow and the fluid flow affects the structural deformation. We impose an inlet condition,

$$\mathbf{u}(0, y, z) = \frac{16 u_{max} y(w - y) z(z - h)}{w^2 h^2} \qquad (4.1)$$

at the inlet and zero pressure condition $p = 0$ at the outlet $p(L, y, z)$, where L is the length of the tank. Here u_{max} represents the maximum velocity along the inlet boundary, and w and h represent the width and height of the flow tank, respectively. We impose this inlet condition such that $u(0, 0, z) = u(0, y, 0) = 0$ and $u(0, \frac{w}{2}, \frac{h}{2}) = u_{max}$. Since the problem is steady state, we are therefore considering the following system of equations:

$$\rho_f (\mathbf{u} \cdot \nabla \mathbf{u}) - \mu \nabla \cdot (\nabla \mathbf{u} + \nabla^T \mathbf{u}) + \nabla p = \mathbf{f} \tag{4.2}$$

$$\nabla \cdot \mathbf{u} = 0 \tag{4.3}$$

$$-\nabla \cdot \sigma = \mathbf{F}_v \tag{4.4}$$

where ρ_f, μ f, and F_v are as defined in chapter 3.

4.2 Numerical Set-up

4.2.1 The Benchmark Sphere

In order to study the interaction between the fluid with the flexible body, we will first analyze the results of laminar flow around a sphere (see figure 4.1). This problem is a classic problem in fluid mechanics [4]. We are primarily concerned with what numerical parameters result in accurate solutions to the Navier-Stokes Equations.
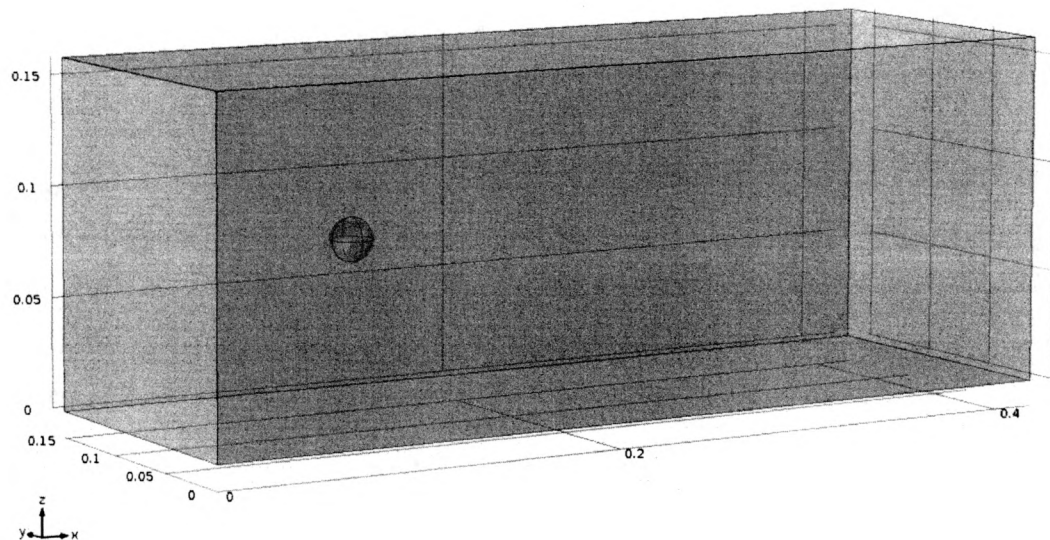
Figure 4.1: Environment used to numerically simulate flow around a rigid sphere in 3-D

The numerical procedure used in Comsol to solve the laminar flow problem is the finite element method. A comparison of discretizations is used between $P1 + P1$ and $P2 + P1$ for fluid elements. $P1 + P1$ means that we construct linear test functions for velocity and linear test functions for pressure, versus $P2 + P1$ using quadratic test functions for velocity. Similar to the 2-dimensional model, we construct a mesh study to analyze the best possible mesh for use in the full ball and fiber model. The mesh study run includes number of mesh elements ranging from 5000 to 310000.

25
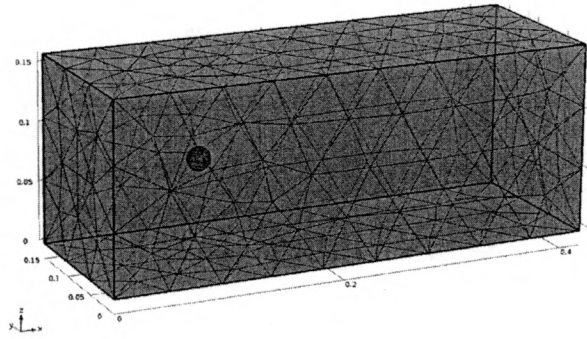
(a) Visualization of the mesh used on the flow tank for the flow around a sphere problem. The mesh was generated with 5847 mesh elements on the domain.
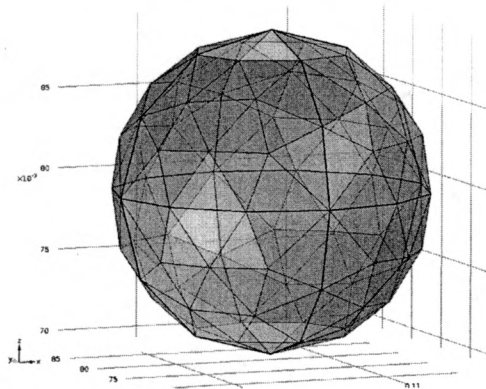
(b) Mesh of the sphere used for the benchmark problem

Figure 4.2: A typical mesh generated by Comsol to solve the 3-D flow past a sphere laminar flow problem.

Drag is chosen as the primary source of comparison for the mesh study. It is well known that for a sphere:

$$F_D = \frac{1}{2}\rho\pi R^2 C_D U^2 \tag{4.5}$$

where F_D, ρ, R, C_D, U are the drag force, density of the fluid, radius of the sphere, drag coefficient, and terminal velocity, respectively. Special attention is paid to the drag coefficient. According to literature drag coefficients of many objects have been both experimentally and numerically computed. Since the velocity is approximated, so is the drag coefficient. There is a known "theoretical" drag curve which tells how the increase in Reynolds number affects the drag coefficient. [6]
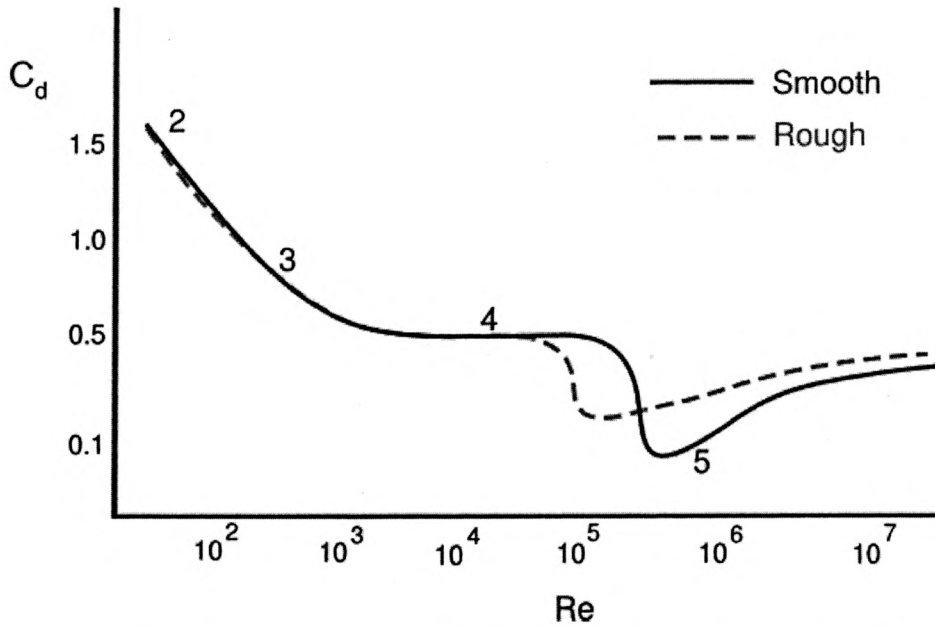
Figure 4.3: The theoretical drag curve for a sphere. Shown are the effects of surface roughness on the drag coefficient. In our study, we consider the sphere to be perfectly smooth.

As a balance between computational time and velocity, we choose parameters that give a Reynolds number of 15000. Specifically, the velocity is chosen to be a slightly higher velocity than the maximum velocity needed in the three-dimensional simulation with sphere and fiber.

$$Re = \frac{ULρ}{μ} \tag{4.6}$$

For this numerical comparison of drag coefficients we use, $μ = 10^{-3}Pa \cdot s$, $U = 0.75m/s$, and $ρ = 1000kg/m^3$. The radius of the ball is $r = 1cm = .01m$. Here, the diameter of the sphere is used as the characteristic length, $L = 2r = .02m$. Estimates have been made for the drag coefficients as a function of Reynolds number. For low Reynolds number the drag coefficient follows a linear relationship with Reynolds number (Stokes flow). There is a point where the drag coefficient increases with increased Reynolds number and then eventually drops off. For higher Reynolds number many papers have been published that attempt to develop an equation governing the relationship between these two variables. Unfortunately, the chosen Reynolds number

27

lies in the regime of instability (the drop-off) for drag coefficients. There are many papers with estimates for the drag coefficients. One in particular points out a list of drag coefficient formulas [6]. Simulations were run for both quadratic and linear velocity elements. In Figure 4.5 we compare the percent error in each formula for drag coefficients to our numerically computed drag for linear velocity elements:
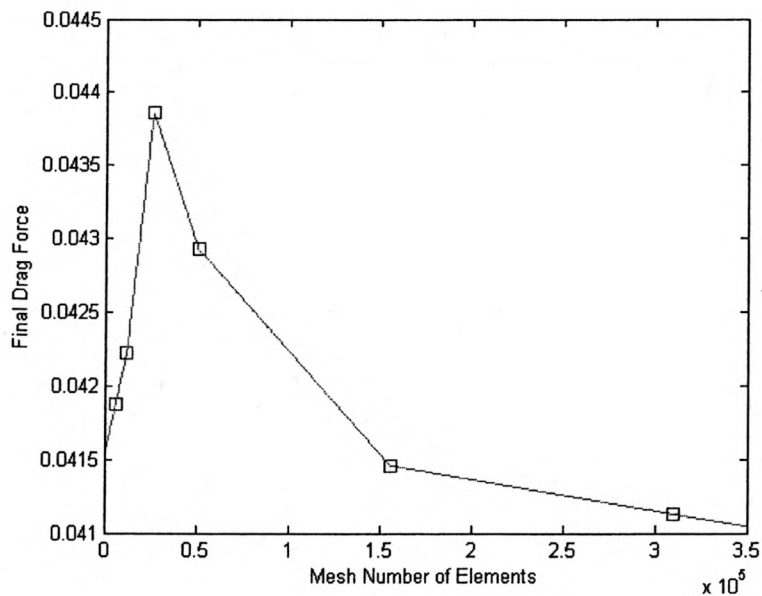
Figure 4.4: Evolution of drag force with increasing mesh elements

Comparisons of Measured and Theoretical Drag Coefficients
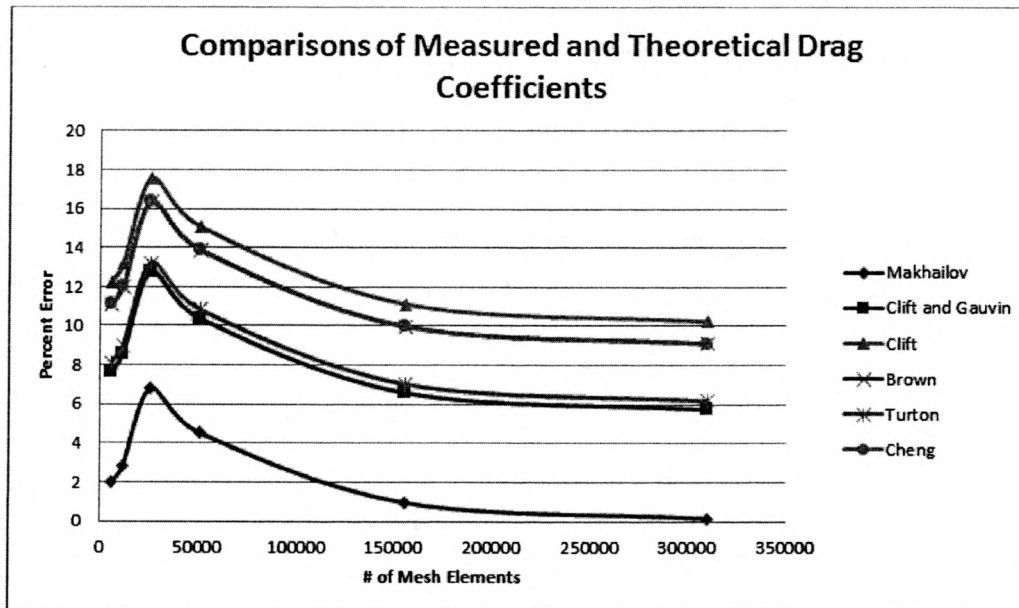
Figure 4.5: Comparison of computed and theoretical drag coefficients based on literature.

Notice here that the smallest percent error lies in the bottom-most theoretical drag formula from Mikhailov [25]. According to Mikhailov:

$$C_{D_A} = \frac{3808\left((1617933/2030) + (178861/1063)Re + (1219/1084)Re^2\right)}{681Re\left((77531/422) + (13529/976)Re - (1/71154)Re^2\right)} \quad (4.7)$$

This formulation of drag coefficient is then used as the standard for our model. Using this reveals small errors for large number of mesh elements.

We can see from Figure 4.1 that the increase of mesh elements greatly reduces the amount of error in the measured drag coefficients relative to the computed drag based on that in literature. Remarkably, the drag for linear velocity elements reaches a point where the error is under 1%. On the other hand, we can see that the error in quadratic elements is still large comparably.

29

Mesh Number of Elements	C_D $P1 + P1$	C_D $P2 + P1$	% Error $P1 + P1$	% Error $P2 + P1$
5847	0.473984641	.581115839	1.97127	25.01907161
11771	0.477832654	.533478156	2.79912	14.77048019
26030	0.496393657	.520264826	6.79226	11.92781398
50843	0.48586821	.506749019	4.52786	9.020074388
155780	0.469231214	N/A	0.94864	N/A
309889	0.465496378	N/A	0.14514	N/A

Table 4.1: Comparison between drag coefficients for varying mesh densities. In this second and third column the drag coefficients are compared between linear and quadratic velocity elements. The percent error is computed relative to the closest representative drag coefficient given in Equation 4.2.1 . The percentage error is also compared between linear and quadratic velocity elements.

Mesh size	DOF $P1 + P1$	DOF $P2 + P1$	Comp. time (s) $P1 + P1$	Comp. time (s) $P2 + P1$
Extremely Coarse	4264	24688	17	120
Extra Coarse	8768	51077	21	202
Coarser	19428	114129	37	1926
Coarse	37360	221797	60	4122
Normal	111576	672291	262	N/A
Fine	218836	1328473	921	N/A

Table 4.2: Comparison of linear and quadratic velocity elements. The pressure is consistently measured in linear test functions. Degrees of freedom (DOF) is compared against computational time and mesh sizes. The mesh sizes correspond directly to the elements of Table 4.1.

These experiments were run with a Intel Xeon CPU E5-2609 v2 with 2 processors at 2.50 GHz each. The CPU holds 8 cores and has 64 GB of RAM. The high percentage error in P2+P1 is considered a practical justification in choosing P1+P1 elements for the discretization of the finite elements needed for the sphere with fiber. It is obvious that for "Fine" mesh size the

rees of freedom is well beyond 1 million degrees of freedom. This is a computationally difficult task to numerically solve.

4.2.2 Convergence Study for Sphere and Fiber

It is the goal of this section to describe the set-up needed to solve the equations governing the 3-dimensional fluid-structure model described in Chapter 2. The environment in which we set-up the fiber attached to basal body is seen in figure 4.6.

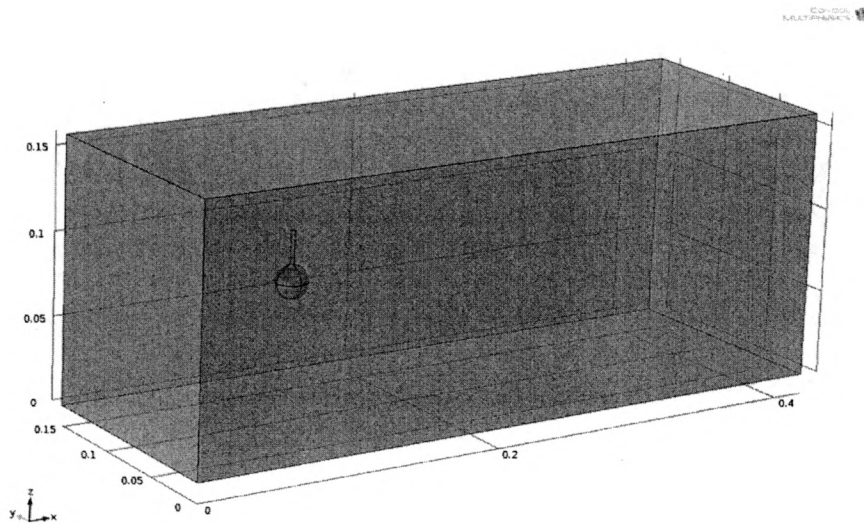Figure 4.6: The sphere with fiber attached in the flow tank. The dimensions of the flow tank are representative of the experiments done and can be seen in the appendix.

The previous section is considered justification in the choice of $P1 + P1$ discretization. The environment must be meshed in order to evaluate the independent variables. To make the proper choice of mesh a mesh study is done for the sphere and fiber.
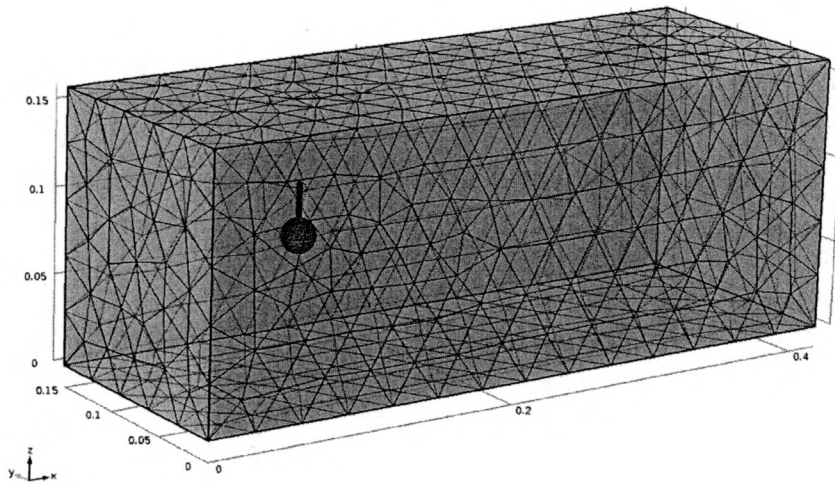
(a) A mesh generated by Comsol of the boundary of the flow tank with ball and fiber inside.
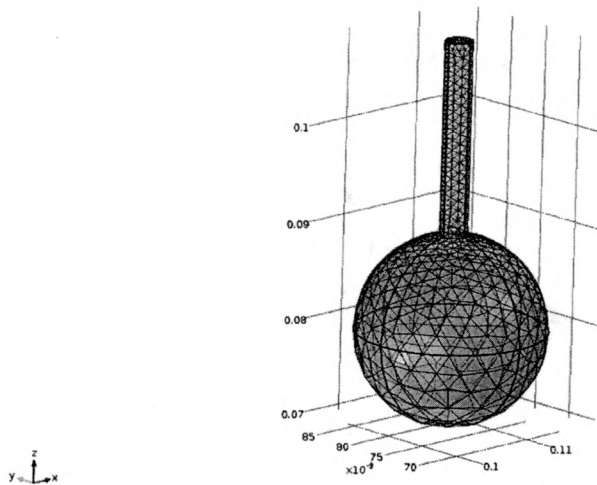
(b) A refined mesh is created around the boundary of the object to ensure that sharp corners are properly dealt with.

Figure 4.7: Meshing of the flow tank with the sphere and fiber.

Three settings governed the meshing of the fluid environment: (1) A Master size defining global properties, (2) Free Tetrahedral meshing for the Flow tank without the fiber, and (3)Free Tetrahedral meshing for only the sphere and fiber. We choose (by trial and error) to make the Master setting a "custom" mesh. The parameters for the custom mesh are detailed in Table 4.3.

Element Size Parameters	Value
Maximum element size	0.00824 [m]
Minimum element size	0.001 [m]
Maximum element growth rate	1.13
Resolution of curvature	0.5
Resolution of narrow regions	0.8

Table 4.3: Custom mesh parameters chosen for Master size in mesh.

According to an official Comsol Multiphysics blog by Andrew Griesmer, to increase performance it is desirable to lower the minimum element size, lower the resolution of curvature, raise the resolution of narrow regions, and increase the maximum element growth rate.[15] This explains the use of certain parameters in the custom mesh given in Figure 4.3.

The mesh governing the ball and fiber is consistently chosen to use the predefined "extra fine" setting in Comsol. This gives a nice refinement near the object to ensure that sharp corners are taken into account. We run a mesh study on the size of the mesh governing the flow tank without the ball and fiber. This parameter sweep runs through four predefined settings with number of elements ranging from 21000 to 74000. Table 4.4 shows us the measured drag at a maximum velocity of $0.4510m/s$ run for each setting of mesh densities. Additionally this table shows the correspondence between degrees of freedom and mesh density. The degrees of freedom is very important in terms of computational time and can result in lack of convergence from matrices of sizes which are too large.

Mesh Elements	Degrees of Freedom	F_D
21617	117209	.02097
31004	167124	.0221
48493	250784	.02251
73857	373838	.02282

Table 4.4: Mesh Study for ball and fiber

In order to measure the relative error, we desire equally spaced mesh points. To do this we use the curve fitting toolbox in Matlab to fit the data. Specifically, Matlab used an interpolant with the Shape-preserving (PCHIP) method interpolating as a piecewise polynomial where the independent variable, number of mesh elements, is normalized by mean 4.37×10^4 and standard deviation 2.296×10^4. This fit is then used to measure the drag at equidistant number of mesh elements. A step-size of 10000 mesh elements is chosen to measure relative drag; that is,

$$Error_{rel} = \frac{|(F_D^{i+1} - F_D^i)|}{|F_D^i|} \tag{4.8}$$

Mesh number of elements	Relative Error
10000	0.0301
20000	0.0637
30000	0.0146
40000	0.0075
50000	0.0066
60000	0.0048
70000	0.0020
80000	0.0017

Table 4.5: Relative Error in drag force measured from interpolated fit.

Mesh Density	Relative Error (N)
21617	0.0605
31004	0.0134
48493	0.0068
73857	0.00071022

Table 4.6: Relative error in drag force for specific values of available mesh densities.

We can see from Table 4.5 that, according to the interpolated fit, the relative error in drag force decreases with increase in mesh density. Figure 4.8(a) shows the increase in the final drag force, measured once the velocity is in steady state and the fiber is

fully deformed, as the mesh density is increased. Additionally, Figure 4.8(b), shows the error described here in increments of 10000 number of mesh elements. On the other hand, the actual available mesh densities for use in Comsol are described in the first column of Table 4.6. The relative errors in drag are also measured for these mesh densities according to the interpolated fit given in Matlab.
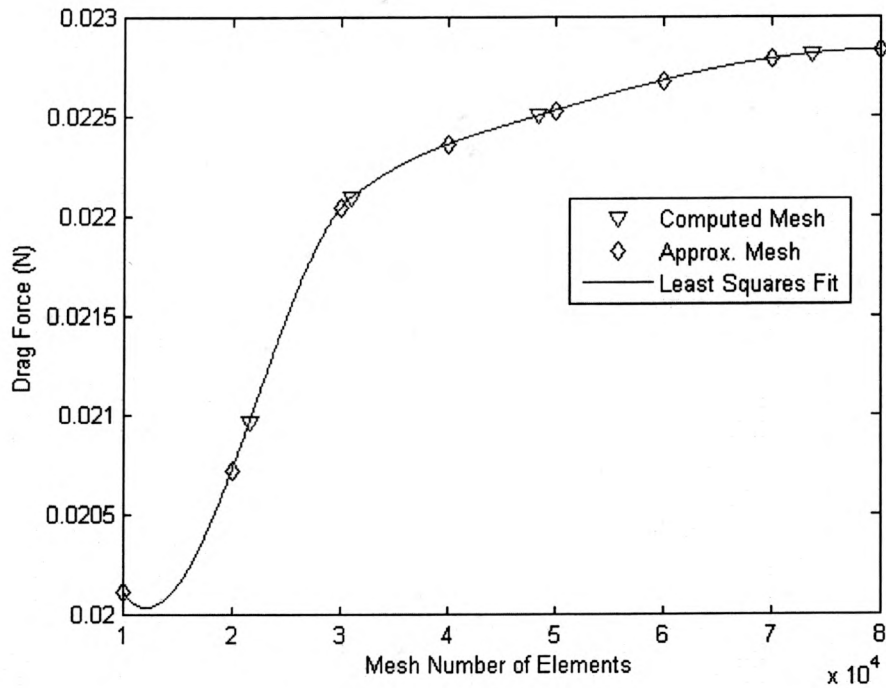
(a) Computed value of final drag force (steady state) with increasing mesh density
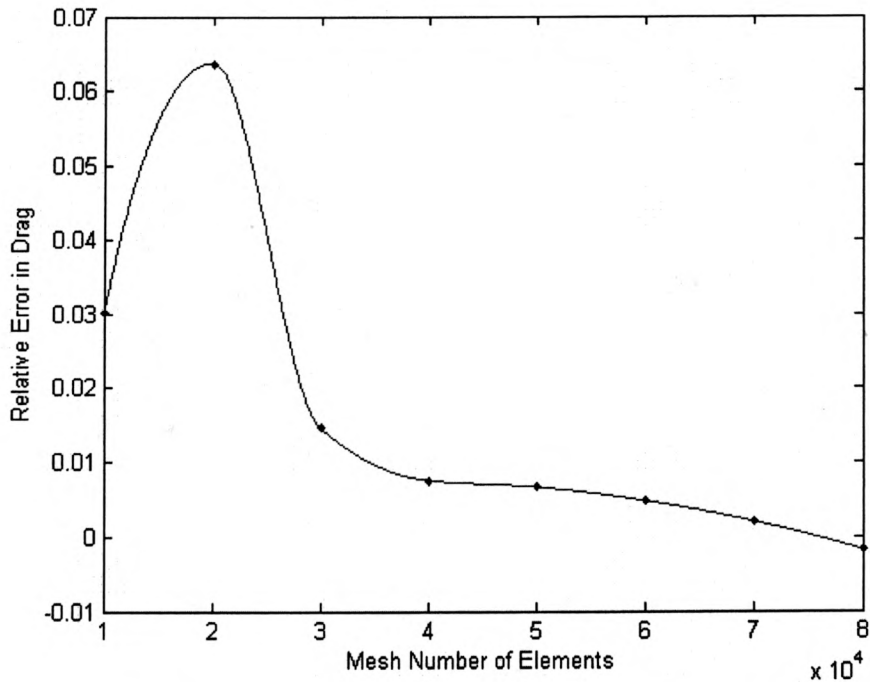
(b) Relative error in drag force according to Equation 4.8.

Figure 4.8: Interpolated fit for mesh study. The blue triangles represent points at which Comsol computed a solution for the given mesh points in Table 4.4 and the black diamonds represent points at which the relative error was measured.

Notice here that the relative error is eventually of order 10^{-3} for a sequence of large mesh densities, which is desirable for convergence. Therefore, the justification in choosing 48493 mesh elements as the number of discretized points to solve on is that the error drop below 10^{-3} for actual values seen in Table 4.6.
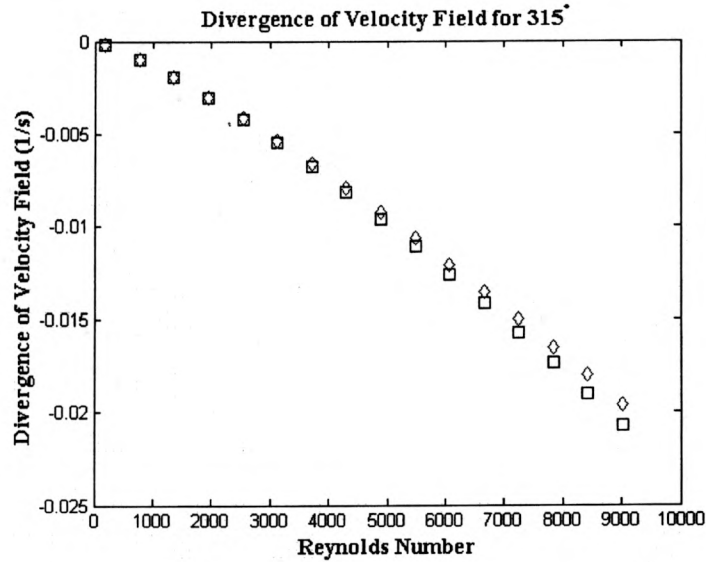
(a) Divergence of Velocity field in 315° initial configuration.
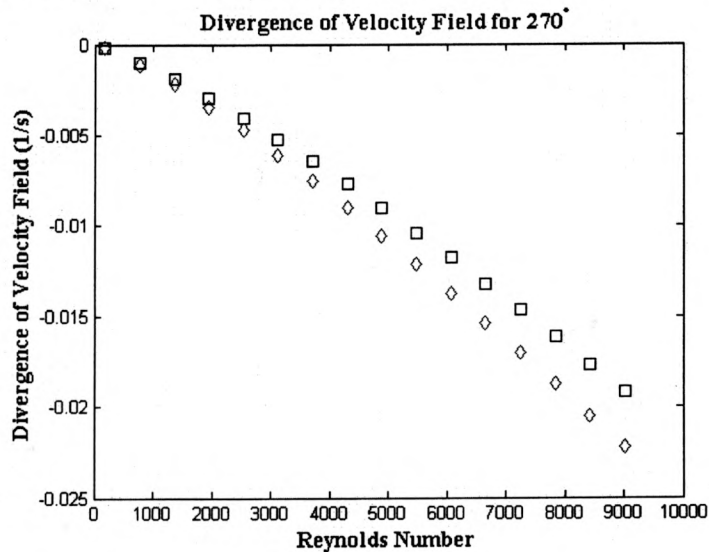
(b) Divergence of Velocity field in 270° initial configuration.

Figure 4.9: Comparison of numerical error in the continuity equation for varying initial configuration angles. Here (□) represents $2cm$ fiber length and (◇) represents $4cm$ fiber length.

A probe was used to calculate the evolution of the divergence of the velocity field throughout the iterations. Figure 4.9 shows the final divergence, after the velocity has reached steady state. We conclude that magnitude of divergence increases with Reynolds number. As we increase Reynolds number we approach turbulence, in which Laminar flow is no longer completely accurate. This plot shows us the error we obtain with said approach to turbulence.

4.2.3   Sphere and Fiber with Chosen Parameters

A study was then computed with a sphere and fiber with chosen parameters, seen in the appendix. Based off the benchmark and convergence studies done, we chose $P1 + P1$ for the discretization of velocity elements and 48493 as the number of mesh points on which to solve the coupled system of equations.

The system of equations (4.2 through 4.4) are used with the same inlet conditions described in Chapter 4.1. The no-slip boundary conditions are imposed on all faces of the rectangular prism and at all boundaries on the ball and fiber and zero pressure conditions are held at the outlet. The sphere is held fixed, while the fiber is free to bend. The tip of the fiber has an imposed boundary load

$$\sigma \cdot \mathbf{n} = \mathbf{F_v} \tag{4.9}$$

where F_v is force per unit volume on the fiber. The fiber is considered to be linear elastic material with isotropic material properties $E = 8 \times 10^6 Pa$, $\nu = 0.33$, and $\rho = 7850 kg/m^3$ being the Young's modulus, Poisson's ratio, and density, respectively. A moving mesh is used as a continuously deforming geometry (like the 2D case) using the arbitrary Lagrangian-Eulerian (ALE) technique. The deformation of the mesh relative to the initial shape of the domain was computed using Winslow smoothing (the default smoothing given by Comsol). The moving mesh again follows

the deformations of the fiber, so to represent the bending, and on the flow tank the deformation was set to zero in all directions. The discretization of the displacement field for the solid is given by quadratic elements.

A fully coupled numerical procedure is used to solve the system of equations. Comsol uses the finite element method to convert the problem from a system of partial differential equations to a system of equations via the stiffness matrix. That is we desire to solve the equation:

$$Ku = b \tag{4.10}$$

where K is the stiffness matrix, $\mathbf{u}$ is the velocity vector and b is the remaining component left over form turning the problem into variational form. In order to solve this linear system we use the MUMPS Linear solver. We assign Newton's method to minimize the quadratic function

$$\mathbf{r}(\mathbf{u}) = \mathbf{bu} - \frac{1}{2}\mathbf{Ku} \cdot \mathbf{u} \tag{4.11}$$

MUMPS then finds the point $f(\mathbf{u}) = 0$, where $\mathbf{r}(\mathbf{u})$ is a minimum. Essentially, we demand that Comsol directly solves the fully coupled system by finding $\mathbf{u} = \mathbf{K^{-1}b}$. Attempting to invert a large matrix can be difficult computationally. This is why special attention was paid to the parameters in this study.

Two different angles were computed for speeds ranging from $0.009m/s$ to $0.4510m/s$, chosen based on the two-dimensional simulations and experiments. Additionally, simulations were run for both $2cm$ and $4cm$ fibers (see figure 6.2).

4.3   Results

As stated in Chapter 2, this three-dimensional simulation is very challenging. In this section, we describe the numerical solutions generated with Comsol. Additionally, we

discuss similar results to the two-dimensional simulations such as deformation angles, drag and lift, and Vogel exponents. Additionally, we show the three-dimensional vortices formed.

4.3.1 Analysis of Drag and Lift

We can see from Figure 4.10 that an increase in fiber length leads to a significant increase in drag force. Additionally, we can see how the drag force is quadratically related to velocity. The lines in red represent exponential least squares fits. That is,

$$F_D = C_D U^\alpha \tag{4.12}$$

Matlab's curve fitting toolbox is used once again to find an exponential fit to this model. The drag coefficients and Vogel exponents, α are summarized in the following table:

Fiber Length	2cm	2cm	4cm	4cm
Angle	315 deg	270 deg	315 deg	270 deg
C_D	0.1092	0.0838	0.1231	0.08825
α	1.984	1.98	1.977	1.966

Table 4.7: Summary of least squares fit of Drag to Velocity

We can see from this table that the Vogel exponents are much closer to the tradi-tional expected value for rigid values of $\alpha = 2$. The flexible body appears to be much stiffer, and bends less due to the properties of the solid such as the bulk modulus.
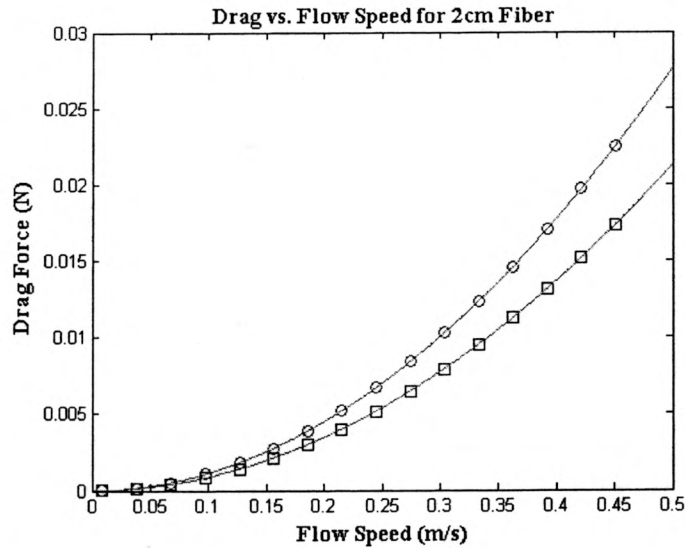
(a) The steady-state drag force on the body for 2cm fiber with increasing flow speed.
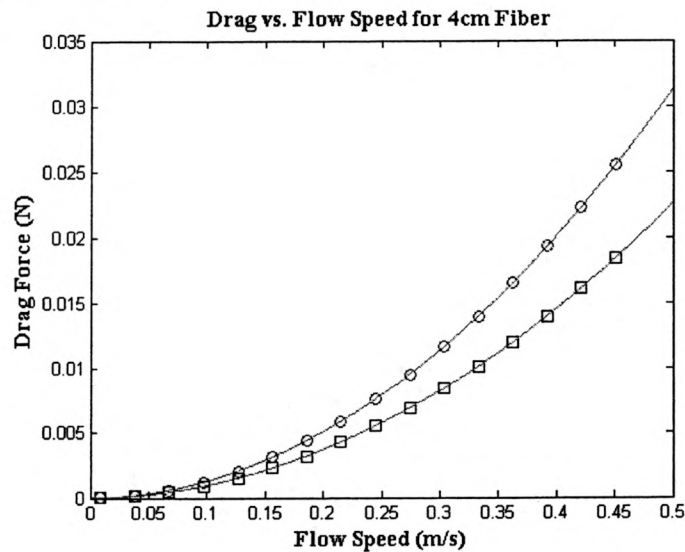
(b) The steady-state drag force on the body for 4cm fiber with increasing flow speed.

Figure 4.10: These plots show the change of drag force as a function of velocity. These plots are computed for angles of 315°(○) and 270°(□)

By definition, the lift force is the force perpendicular to the flow. Since the flow at infinity is in the x direction, we have that the lift force now has two components. This differs from the 2-dimensional model, in which we had only one lift force.
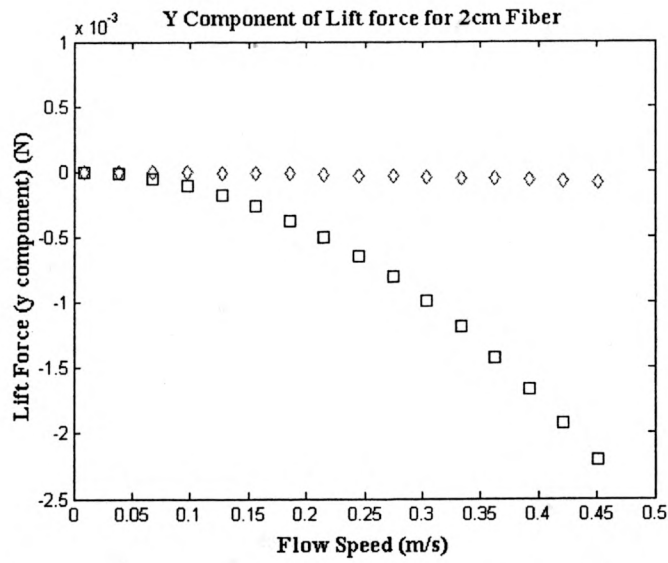
(a) Comparison of Lift y-component for $2cm$ fiber length.
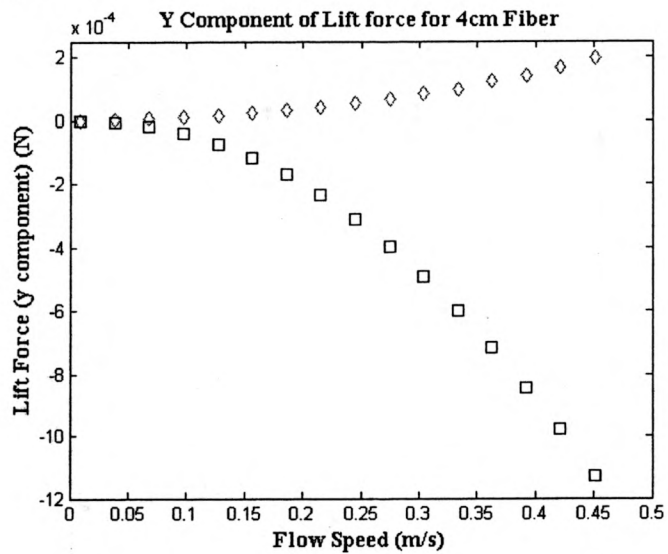
(b) Comparison of Lift y-component for $4cm$ fiber length.

Figure 4.11: The y-component of the lift force is plotted against flow speed. Here the (□) represents 315° and (◇) represents 270° angles.
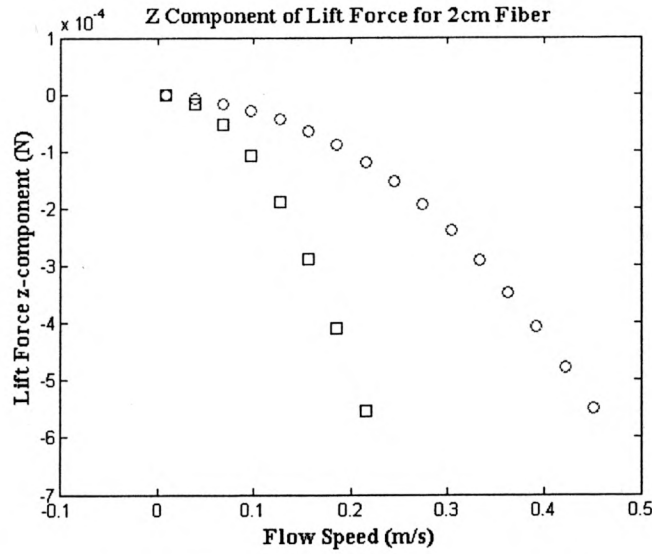
(a) Comparison of Lift z-component for 2*cm* fiber length.
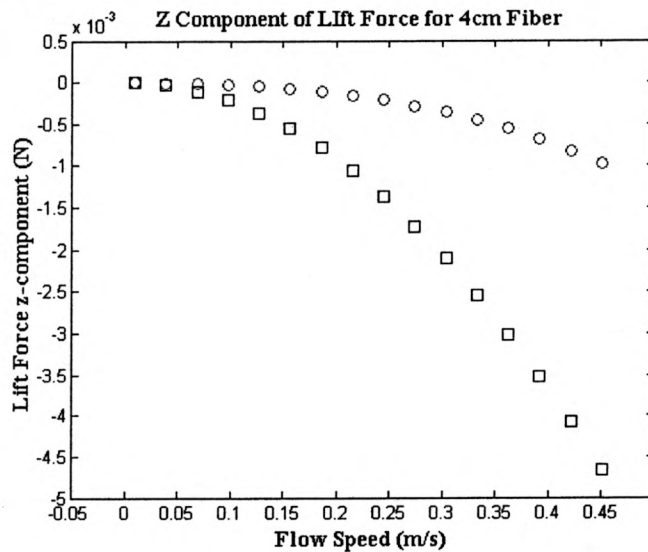
(b) Comparison of Lift z-component for 4*cm* fiber length

Figure 4.12: Z component of the Lift force with comparison in initial configuration angle of the fiber. Here the (□) represents 315° and (○) represents 270° angles.

4.3.2 Analysis of Bending

A main focus in this research was to analyze the bending of fibers under fluid flow. Specifically, it is desirable to understand how changing different lengths of fibers and

initial configuration angles may affect the flow around the fiber. Furthermore, we would like to analyze the vortex affects that occur around them. Some people are interested in how fibers, known as primary cilian (sensors in certain cells), may affect the blood flow around them. This blood flow may affect the calcium intake and therefore affect the cell-division process. It is important, therefore, to understand how different parameters induce bending and flow effects.

Since we are dealing with a three-dimensional model, one must consider the additional angles needed to fully describe the bending of the fiber. It seems natural, in this instance, to use spherical coordinates. The initial coordinates $(x_i, y_i, z_i$ were calculated by hand using the coordinates of the sphere. That is, for the 270 degree case, we have $x_i = x_{sphere}$, $y_i = y_{sphere}$, and $z_i = z_{sphere} + r_{sphere}$. For the 315 degree case we used a geometrical argument to deduce $x_i = x_{sphere} + r_{sphere} \cos(45°)$, $y_i = y_{sphere}$, and $z_i = z_{sphere} + r_{sphere} \sin(45°)$. The coordinates of the tip of the fiber, denoted (x_f, y_f, z_f) were measured using an averaging probe around the boundary representing the tip of the fiber. We will use spherical coordinates, (r, φ, θ), where φ is the measure of the angle from the vertical and θ is the measure of the angle in the xy plane. Typically, the bending in the zx direction, φ, is that being compared to the 2-dimensional results. Here $\theta = \tan^{-1}(\frac{\triangle y}{\triangle x})$ and $\varphi = \cos^{-1}(\frac{\triangle z}{r})$, where $r = \sqrt{\triangle x^2 + \triangle y^2 + \triangle z^2}$.
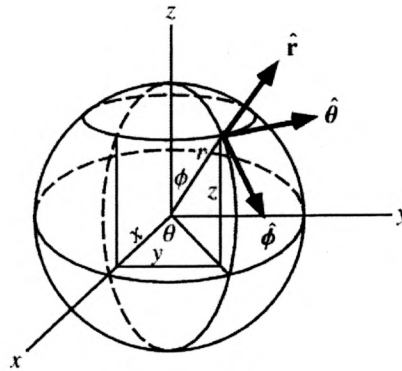
Figure 4.13: A schematic of the deformation angles in 3-D. Picture courtesy of [35].
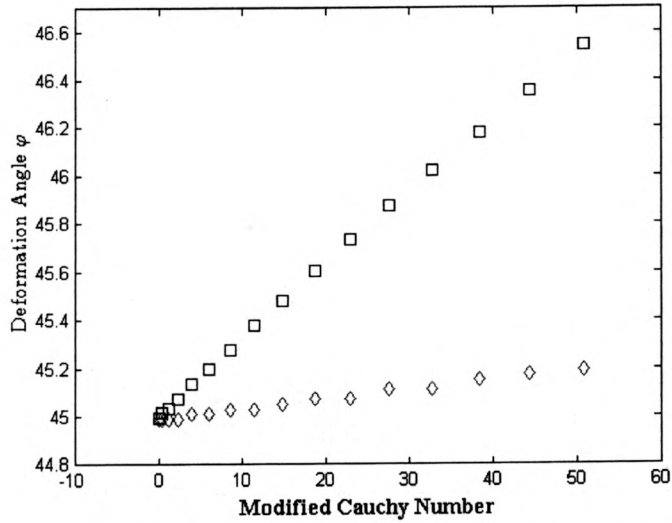
(a) ZX Deformation with initial configuration angle of 315°.
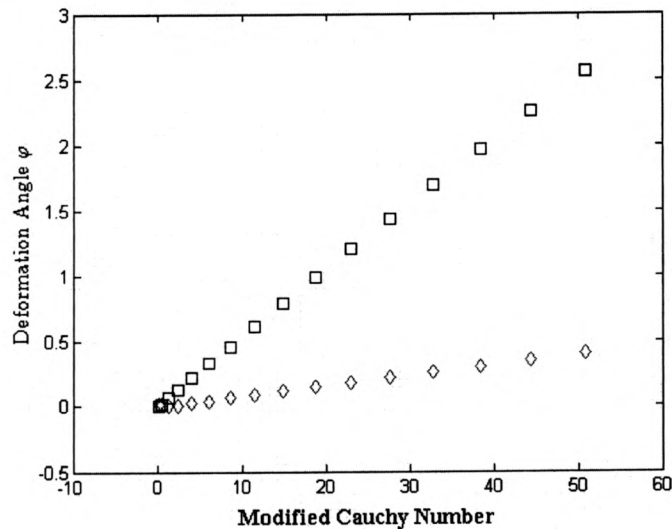
(b) ZX Deformation with initial configuration angle of 270°

Figure 4.14: The φ Deformation is considered to be measured in the ZX plane (up and down). These angles are measured for both 315° and 270° configuration angles for fiber lengths of $2cm$ (◇) and $4cm$ (□).

We can see from Figure 4.14 that an increase in fiber length corresponds to an increase in bending. Furthermore, for higher Cauchy numbers we have that the difference between the deformation angles among varying fiber lengths increases. For Cauchy numbers of about 50 one can see that the difference between the $4cm$ and $2cm$

45

fibers in initial configuration of 315 degrees is about 1.5°. Additionally, the difference in the 270° case seems more significant. The difference between the differing fiber lengths seem to vary about 3° in this case. If we compare among the two images we see that qualitatively the different configuration angles produce qualitatively similar deformation. Although, the difference is subtle, it appears that the 270° configuration changes with modified Cauchy number in a faster rate. A few degrees may be significant on the cellular level. The fiber that we represent here is merely a prototype to represent different scenarios , in which bending may be more. For example, the hair that lines the skin is much thinner than the fiber used, and thus has different structural properties. We expect that these type of fibers should bend more. For the two-dimensional study, we used a fiber of different length and resulted in significant bending. This simulation now shows us that the difference in structural properties can lead to a significant difference in stiffness and therefore bending.

According to the numerical simulations computed, there is no bending in the yx direction, θ, for the 315° case. This means that $\theta = 0$. Interestingly enough, we do have a θ component in the 270° case. The results are shown below.
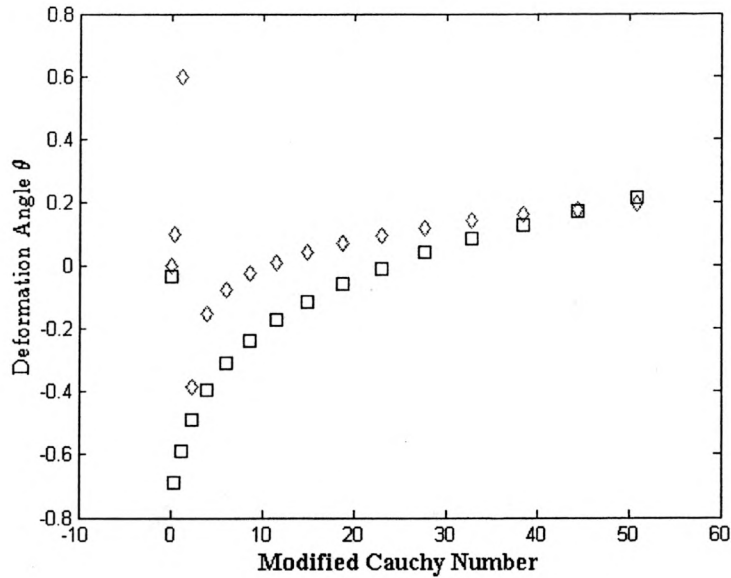
Figure 4.15: θ Deformation is considered to be bending in the yx direction. This deformation was measured with initial configuration of 270°. Here ($\diamond$) represents $2cm$ fiber length and ($\square$) represents $4cm$ fiber length.

In figure 4.15 we see that initially the bending angles drop significantly. We believe this is due to error in the averaging in the coordinates of the tip (x_f, y_f, z_f). Notice, however, how the $2cm$ fiber actually bends more than the $4cm$ fiber for a while. If we examine the graph more closely, we can see that the magnitude of the bending is greater in the $4cm$ case, however. The $4cm$ bends in the opposite direction initially for low Reynolds numbers. Eventually, for large enough Reynolds numbers, the two fibers have an insignificant difference in bending angle θ. This bending in the xy direction is significant in terms of 3-dimensional effects. We have no previously seen a second angle effect. This will later be explained by 3-dimensional vortex effects.

4.3.3 Analysis of Velocity and Pressure

In this section, the solutions to Navier-Stokes equations are analyzed more closely. Both the velocity field and pressure play a significant role in this problem. We see that

the sphere and fiber actually create vortex motion, as seen in the two-dimensional case. A significant difference will be noted. The goal in this section is to show a significant number of viewpoints for the velocity field and pressure. Being a three-dimensional problem many vantage points can be taken. The following images were taken with $4cm$ fiber in both 90° and 45° configurations at a maximum flow velocity of $.4510m/s$.
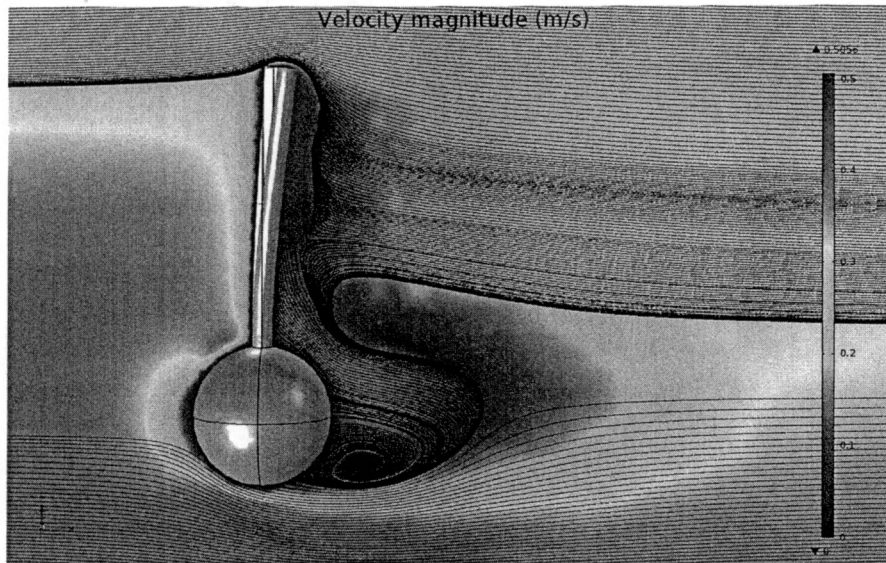
Figure 4.16: The plane viewed in this picture is the zx plane. The fluid flows from to the right in this picture. Red signifies higher velocity and blue signifies lower velocity. The color code measures the magnitude of the velocity vector at each point of the plane. The black lines represent the projection of the streamlines of the flow onto the zx plane and were computed at the position of the body. If $\mathbf{u} = (u_x, u_y, u_z)$, then here $u_y = 0$.
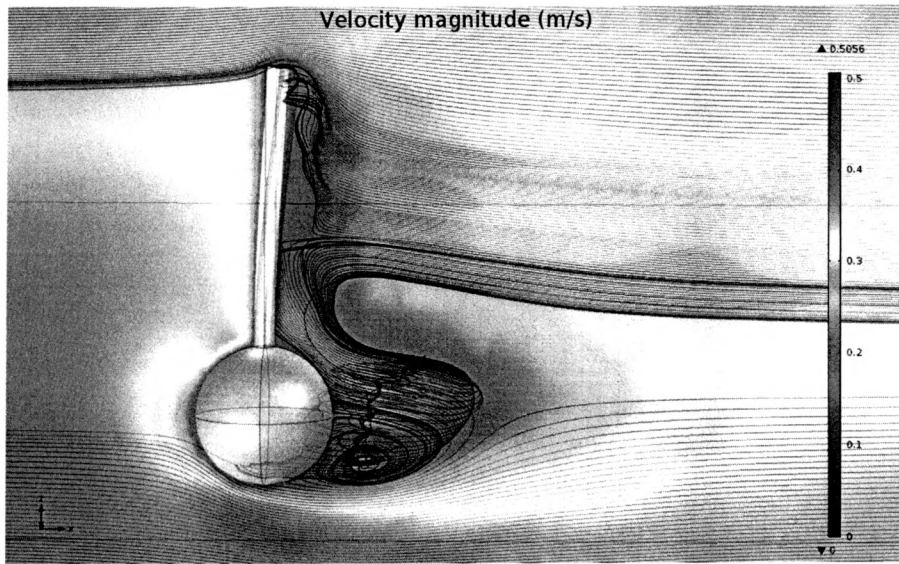
Figure 4.17: This picture is similar to the previous picture except that the streamlines are viewed with all three components. Here the three-dimensional vortex structure is apparent. The velocity profile is taken to be slightly opaque to visualize the streamlines behind the body.
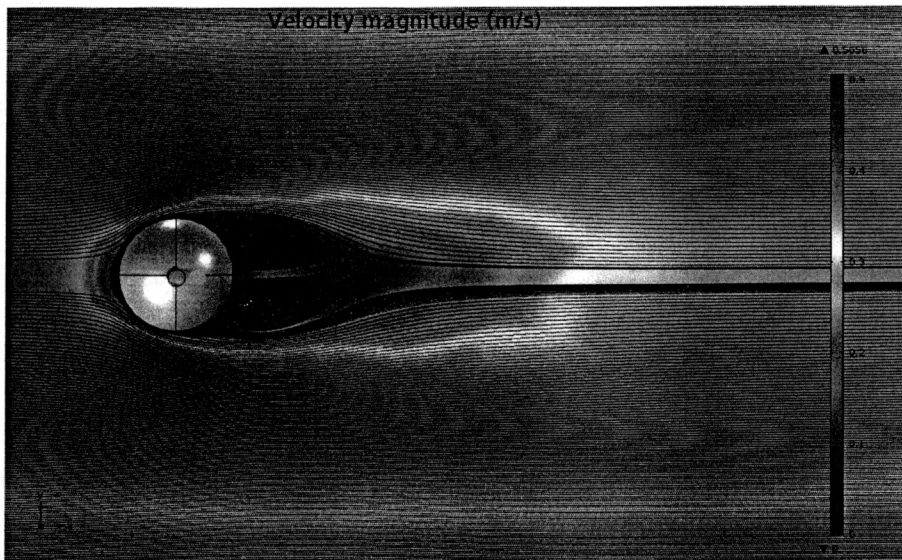
Figure 4.18: This picture shows the aerial view (above the fiber) of the flow velocity plane (yx) with streamlines following the flow (left to right). The streamlines here are projected on to the yx plane ($u_z = 0$) and show similar results to the flow past a rigid cylinder problem.

Figure 4.19: Pressure gradient on the ball and fiber seen in a contour plot.

Chapter 5

Comparisons between 2D and 3D

One main goal in computations is to reduce the dimensionality of the problem to make the modeling easier. It is important to check the validity of this reduction, however. We will outline comparisons between the simulations in two and three dimensions here.

In the two-dimensional experiments we see the Vogel exponents to be significantly smaller than those of the three dimensional problem. In 2-D we see Vogel exponents ranging from 1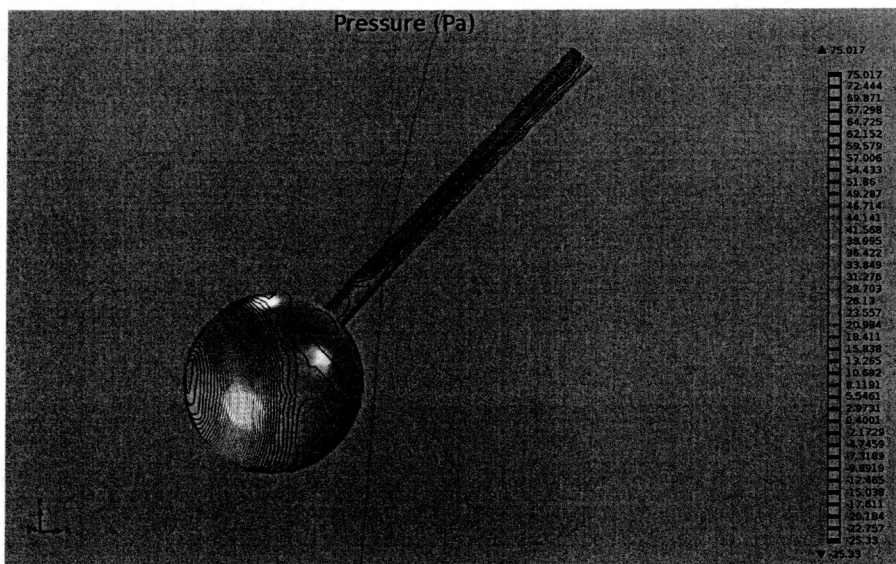.1 to 1.4. In 3-D we see that the Vogel exponents follow closer to the exponents of a rigid body. Specifically we have found that the exponents range from 1.96 to 1.99. There appears to be a difference between rigid bodies. The flexibility of the fiber does appear to partake a primary role in this analysis. Since the Vogel exponent holds all the information needed for drag we use this as our comparison of the drag force between the differing dimensions.

The deformation in the zx plane was measured (φ) in both two and three dimensions. We have found there to be insignificant differences in the percent increase in bending between the slowest flow speed of $u = .009m/s$ and fastest flow speed of $u = 0.4510m/s$. We measured the initial configurations of 270° and 315° for both the $2cm$ and $4cm$ fibers. For the $2cm$ fiber the percentage increase in bending is rather

Angle	2D %	3D %
270°	0.50908	0.147211349
315°	0.19281	0.064313345

Table 5.1: Percentage increase in $2cm$ fiber length bending at $u = 0.4510m/s$ relative to $u = 0.009m/s$ for initial configurations of 270° and 315° for both 2-D and 3-D simulations.

Angle	2D %	3D %
270°	4.66557	0.946241708
315°	1.61049	0.492157133

Table 5.2: Percentage increase in $4cm$ fiber length bending at $u = 0.4510m/s$ relative to $u = 0.009m/s$ for initial configurations of 270° and 315° for both 2-D and 3-D simulations.

small. Specifically, for 270° we see an increase of about 0.5% in 2-D versus an increase of approximately 0.14% for 3-D. The 315° initial configuration shows an percentage increase of approximately 0.19% for the 2-D fiber versus an increase of approximately 0.064313345% for the 3-D fiber. The $4cm$ fiber bends much more however, but shows no significant difference in dimensionality. For the initial configuration of 315° we have an percentage increase of about 4.7% for 2-D fiber and 0.95% for 3-D fiber. For the initial configuration of 270° we see an increase of approximately 1.61% for the 2-D fiber and 0.49% for the 3-D fiber. More accurate calculations and relative percentage differences are seen in tables 5.1 and 5.2.

Finally, a comparison is made between the dimensions of the vortices formed behind the solid body. Significant attention is paid to the dimensions of the vortex structure formed behind certain bodies [[8],[5]] In two dimensions we measured the length and height of the vortices and compared them relative to the length and width of the flow tank, respectively. In three dimensions we measured the length,width, and height of the vortices relative to the length,width, and height of the flow tank, respectively. In this section we compare both 315° and 270° configurations for initial maximum flow speed of $u = 0.4510m/s$. Since the $4cm$ appear to have more interesting effects

Vortex Dimensions	Relative % 2D	Relative % 3D
315° *Length*	23.72396898	39.9304678
315° *Width*	N/A	4.81269387
315° *Height*	39.9304678	22.67716535
270° *Length*	17.45537829	6.50680029
270° *Width*	N/A	16.20734908
270° *Height*	27.77535882	15.11811024

Table 5.3: Comparison between two-dimensional and three-dimensional vortex dimensions for 315° and 270° initial fiber configurations.

than the $2cm$ fiber, we outline the information for only the $4cm$ fiber. According to the measurements taken in two-dimensions, the relative length of the vortex to the length of the tank is approximately 23.7%, whereas the relative height of the vortex to the relative height of the tank is approximately 40% for 270° initial configuration. The corresponding 315° measurements taken approximate the relative length and width to be 17.46% and 27.8%, respectively. On the other hand, for the 270° initial configuration, the approximate length, width, and height of the vortices relative to the dimensions of the tank are 4.81%, 13.1%, and 22.7%, respectively. The 315° relative length, width, and height, are approximately 6.51%, 16.2%, and 15.1%, respectively. Although there appear to be differences in the lengths and heights of the vortices formed behind the solid object, the hypothesis is that the structural parameters (such as the bulk modulus) contributes greatly to these effects. These parameters were changed in 3-D to more accurately depict the experiments performed.

Chapter 6

Conclusion

In conclusion, our goal with this study was to investigate how fluids interact with elastic fibers. We aimed to show how the initial configurations effect the final configurations and the forces upon these fibers.

In the second chapter we described the experimental procedure. We experimentally measured the bending of these fibers and have seen, generally, that longer fibers bend more. We notice a difference in the magnitude of bending, both experimentally and numerically between the different initial configurations. Specifically, the fiber experiences the most bending when the fiber is pointed straight upwards in the $\hat{z}$ direction (initial configuration of 270°. The experiments reveal that there is a certain critical value of Ca where the fiber starts to bend. Eventually this bending is controlled by time-dependent motion, for high enough Ca. The laser imaging (Figure2.3) reveals the vortex-like flow pattern formed behind the basal body. This imaging indicates complex wake vortex pattern occurring even for fairly low velocities.

Comsol was then used to numerically simulate this phenomenon. The primary source of comparison was chosen to be the drag force on the body. We analyzed the effects of the mesh density, height, and size of the ball in terms of the drag force. Convergence in 2-D was analyzed and an appropriate mesh was chosen. The

channel height seems to affect the drag and lift forces significantly. The height in the experiments were fixed, however, and were chosen to dictate the simulations. The size of the ball seems to have a significant effect with initial configuration of 225°, but less so with the other configurations. The deformation seems to match closely to the experiments for the $2cm$ fiber, exhibiting little to no bending. We see, additionally, that longer fibers are more prone to bending than the shorter ones. The orientation has an effect on the bending of the fiber. The deformation angle is largest when the fiber faces into the flow and least when the fiber is more streamlined. The Vogel exponents (drag exponents) seem to match to the ranges reported in literature.

A similar study was developed numerically in 3-D (see chapter 4) to compare the differences. The goal was to see if their were any qualitative differences in the flow. Since the parameters of the experiment were changed to more realistically represent the experiments, we expected some change. Specifically, we have found the relative change in deformation from lowest to highest speed is not significantly different from 2-D to 3-D. The $2cm$ fiber still seems to have low deformation, which matches experiments. Qualitatively, the longer fibers still experience more drag and bend more than shorter fibers. The initial configuration angle seems to have a significant effect on the bending. The 270° configuration shows more deformation than the 315° case for both $2cm$ and $4cm$ length fibers. The 3-D simulations reveal an additional bending angle, θ. Although the scale of this bending is small, alternative bending angles cannot be neglected until further investigation is done. This additional bending may very well come from the additional component of the lift force in the y direction. Once again, the scale of this force is small ($O(10^{-3})$) but further analysis may prove this value non-negligible. Since the parameters of this three-dimensional study have been modified we see an increase in Vogel exponents. Specifically we see exponents in the range of $1.96 - 1.99$. These seem to match closely to the drag exponents of rigid bodies. This explains the lack of deformation in the φ direction.

A stiffness parameter study should be done to analyze the difference in bending. Future work would include the analysis of stiffness, the effect of fluid viscosity, and effect of the material on the sphere. In future work we intend on numerically computing the transient terms in the system 4.2 such as to obtain an understanding of the build up to steady state. Understanding the time-dependent three-dimensional model will help analyze such things as vortex shedding and flapping. In future work, a critical speed study would be done to see, for different material properties, at what speeds the fibers begin to flap. The determination of the proper dimension to analyze the experiments is of utmost importance. The hope is that, with additional investigation, this fluid-structure interaction problem can be modeled as much as possible with numerical simulations.

Bibliography

[1] Alben, S., Shelley, M. and Zhang, J., Drag reduction through self-similar bending of a flexible body, Nature, 420, 479-481, 2002.

[2] S. Alben, M. Shelley, and J. Zhang, How flexibility induces streamlining in a two-dimensional flow, Physics of Fluids 16 (5): 1694-1713, 2004

[3] Bertoglio, C., D. Barber, N. Gaddum, I. Valverde, M. Rutten, P. Beerbaum, R. Hose, and J. Gerbeau. "Identification of Artery Wall Stiffness: In Vitro Validation and in Vivo Results of a Data Assimilation Procedure Applied to a 3D Fluid-structure Interaction Model." Journal of Biomechanics 47 (2014): 1027-034. Web.

[4] Batchelor, G.K., An introduction to fluid dynamics, Cambridge University Press, 2000.

[5] Camassa, R., Chung, B.J., Howard, P., McLaughlin, R.M., Vaidya, A., Vortex induced oscillations of cylinders at low and intermediate Reynolds numbers, Advanced in Mathematical Fluid Mechanics, Ed. A. Sequeira and R.Rannacher, Springer Verlag, 2010.

[6] Cheng, N., Comparison of formulas for drag coefficient and settling velocity of spherical particles, Powder Technology, 395-398, February 13, 2009

[7] Childress, S., Mechanics of Swimming and Flying (Cambridge Studies in Mathematical Biology), Cambridge University Press, July 31, 1981.

[8] Chung, B.J., Gipson, G., Shenoy, A. and Vaidya, A., Image analysis of wake structure past cylinders of finite lengths, International Journal of Imaging, Volume 4, A10, 18-32, 2010

[9] Cortes, S., D. Guemes, and R. Avila. COMSOL Conference Boston 2013, Print.

[10] Fields, S.B., Klaus, M., Moore, M.G. and Nori, F., Chaotic dynamics of falling disks, Nature, 388, 252-254, 1997.

[11] Galdi G.P., and Vaidya A., Translational Steady fall of Symmetric Bodies in Navier-Stokes Liquid, with Application to Particle Sedimentation, Journal of Mathematical Fluid Mechanics, 3, 183-211, 2001.

[12] Galdi, G., P., On the Motion of a Rigid Body in a Viscous Fluid: A Mathematical Analysis with Applications, Handbook of Mathematical Fluid Mechanics, Elsevier Science, Amsterdam, 653-791, 2002.

[13] Giordano, Rosaria, Tommaso Astarita, and Giovanni M. Carlomagno. Vortex Shedding in the near Wake of a Finite Cylinder. Proc. of 14th International Symposium on Applications of Laser Techniques to Fluid Mechanics, Portugal, Lisbon, Print.

[14] Gosselin, F., de Langre, E. and Machado-Almeida, B.A., Drag reduction of flexible plates by reconfiguration, Journal of Fluid Mechanics, 650, 319, 2010.

[15] Griesmer, Andrew. Size Parameters For Free Tetrahedral Meshing In COMSOL Multiphysics. COMSOL Blog 2014. Web. 20 Jan. 2015.

[16] Harder, D., Speck, O., Hurd, C. and Speck, T. Reconfiguration as a prerequisite for survival in highly unstable flow-dominated habitats. J. Plant Growth Regul. 23, 98–107, 2004.

[17] Hasnedlová, Jaroslava, Miloslav Feistauer, Jaromír Horáček, Adam Kosík, and Václav Kučera. Numerical Simulation of Fluid–structure Interaction of Compressible Flow and Elastic Structure. Computing 95.S1 (2013): 343-61. Web.

[18] Huang L, Quinn SJ, Ellis PD, Williams JE., Biomechanics of snoring, Endeavour, 19(3):96-100, 1995.

[19] Karimi, Alireza, Mahdi Navidbakhsh, Reza Razaghi, and Mohammad Haghpanahi. A Computational Fluid-structure Interaction Model for Plaque Vulnerability Assessment in Atherosclerotic Human Coronary Arteries. Journal of Applied Physics 115.14 (2014): A Computational Fluid-structure Interaction Model for Plaque Vulnerability Assessment in Atherosclerotic Human Coronary Arteries. AIP Publishing LLC, 11 Apr. 2014. Web.

[20] Kirchoff, G., Uber die Bewegung enines Rotationskorpers in einer flussigkeit, J. Reine Ang. Math. Soc., 71, 237-281, 1869.

[21] Kwon, Young W., and Scott C. Knutton. Computational Study of Effect of Transient Fluid Force on Composite Structures Submerged in Water. International Journal of Multiphysics 8.4 (2014): 367-95. Web.

[22] Leal, L.G., Particle Motion in a Viscous Fluid, Annual Review of Fluid Mechanics, 12, 435-476, 1980.

[23] Luhar, M. and Nepf, H.M., Flow induced reconfiguration of bouyant and flexible aquatic vegetation, Limnology and Oceanography, 56 (6), 2003-2017, 2011.

[24] Lugt, H., Autorotation, Annual Review of Fluid Mechanics, 15, 123-147, 1983.

[25] Mikhailov, M.D., & Freire A.P., The drag coefficient of a sphere: An approximation using Shanks transform, Powder Technology, 237, 432-435, 2013.

[26] Mittal, R., Seshadri, V. and Udaykumar, H.S., Flutter, Tumble and Vortex Induced Oscillations, Theoretical and Computational Fluid Dynamics, **17**, 165–170, 2004.

[27] L.B. Pedersen and J.L. Rosenbaum. Current Topics in Developmental Biology.85:23-61, 2008.

[28] Schouveiler, L., Eloy, C. & Le Gal, P., Flow-induced vibrations of high mass ratio flexible filaments freely hanging in a flow. Phys. Fluids 17 (4), 047104-8, 2005.

[29] Shelley, M.J. and Zhang, J., Flapping and bending bodies interacting with fluid flows, Annual Rev. Fluid Mech., 43, 449-465, 2011.

[30] Slaughter, W.S., The linearized theory of elasticity, Birkhauser, 2002.

[31] Rajani, B.n., A. Kandasamy, and Sekhar Majumdar. "Numerical Simulation of Laminar Flow past a Circular Cylinder." Applied Mathematical Modelling 33.3 (2009): 1228-247. Web.

[32] Tanabe, Y. and Kaneko, K., Behavior of falling paper, Physical Review Letters, 73, 10, 1372-1376, 1994.

[33] Vogel, S., Drag and flexibility in sessile organisms, American Zoologist, 24(1), 37–44, 1984.

[34] Vogel, S., Drag and reconfiguration of broad leaves in high winds, Journal of Experimental Botany, 40(217), 941-948, 1989.

[35] Weisstein, Eric W. "Spherical Coordinates." From MathWorld–A Wolfram Web Resource. http://mathworld.wolfram.com/SphericalCoordinates.html

[36] Wick, Thomas. Coupling of Fully Eulerian and Arbitrary Lagrangian–Eulerian Methods for Fluid-structure Interaction Computations. Computational Mechanics 52.5 (2013): 1113-124. Web.

[37] Willmarth, W.W., Hawk, N.E., Galloway, A.J. and Roos, F.W., Journal of Fluid Mechanics, 27, 177–207, 1967.

[38] Yuan, Q., L. Zhang, D. Xiao, K. Zhao, C. Lin, and L. Si. An Accurate, Flexible and Small Optical Fiber Sensor: A Novel Technological Breakthrough for Real-time Analysis of Dynamic Blood Flow Data in Vivo. PLoS One 9.12 (2014), Web.

[39] Zhu, L., Viscous flow past a flexible fibre tethered at its center pint: vortex shedding, J. Fluid Mech., 587, 217-234, 2007.

[40] Zong, Lijun, and Heidi Nepf. Vortex Development behind a Finite Porous Obstruction in a Channel. Journal of Fluid Mechanics 691 (2012): 368-91. Web.

Appendix

Parameter	Values
Domain Height	0.18 [m]
Domain Length	0.5 [m]
Fiber width	0.0005 [m]
Fiber Length	0.02,0.04,0.06 [m]
x coordinate of cylinder	0.09 [m]
y coordinate of cylinder	0.09 [m]
Radius of disk	0.0125 [m]
Density of solid	10000 [kg/m^3]
Poisson ratio	0.4
Shear modulus	0.7×10^9 [$kg/(ms^2)$]
Young's modulus	2.8 × 10^9[$kg/(ms^2)$]
Fluid density	1000 [kg/m^3]
Fluid kinematic viscosity	0.001 [m^2/s]
Fluid dynamic viscosity	1[m^2/s]
Mean inlet flow	0.009-0.451[m/s]
Reynolds number	0-30,000
Initial angle of the fiber	135°(225°), 90°(270°), 45°(315°)

Table 6.1: The table lists the numerical values of parameters assumed in our 2D numerical investigations.

Parameter	Values
Domain Length	0.4191[m]
Domain Height	.15875[m]
Domain Width	.1524[m]
x coordinate of the sphere	.10478[m]
y coordinate of the sphere	.0762[m]
z coordinate of the sphere	.079375[m]
Radius of the sphere	.01[m]
Radius of the fiber	.0015[m]
Density of solid	7850 $[kg/m^3]$
Poisson ratio	0.33
Shear modulus	3.008×10^6 $[kg/(ms^2)]$
Young's modulus	$8 \times 10^6 [kg/(ms^2)]$
Fluid density	1000 $[kg/m^3]$
Fluid kinematic viscosity	1×10^{-6} $[m^2/s]$
Fluid dynamic viscosity	1×10^{-3} $[m^2/s]$
Mean inlet flow	0.009-0.451$[m/s]$
Reynolds number	0-9,020
Initial angle of the fiber	90°(270°), 45°(315°)

Table 6.2: The table lists the numerical values of parameters assumed in our 3D numerical investigations.
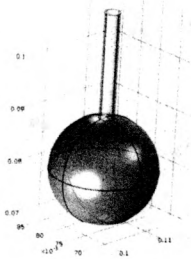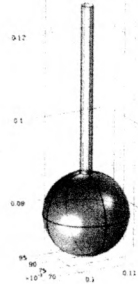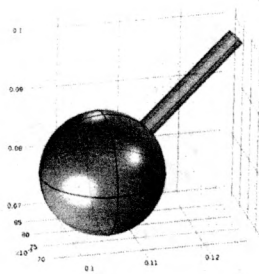
Supplemental Figures
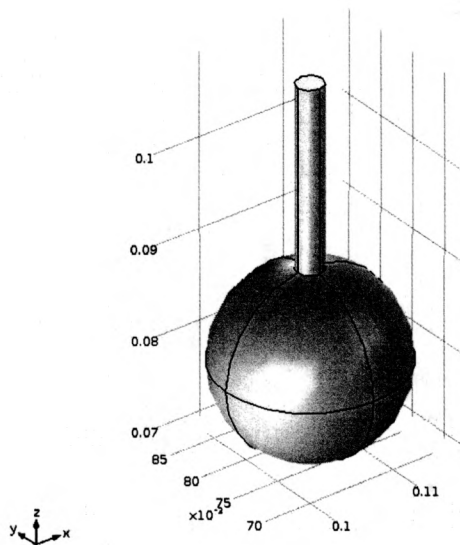
Figure 6.1: Geometrical entity designed in Comsol to model the ball and fiber used in experiments.
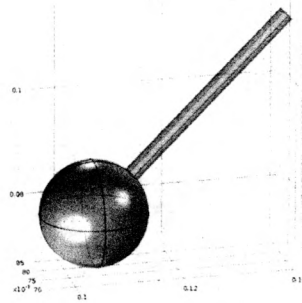
(a) Fiber Length=2cm, Initial angle = 270°

(b) Fiber Length=4cm, Initial angle = 270°

(c) Fiber Length=2cm, Initial angle = 315°

(d) Fiber Length=4cm, Initial angle = 315°

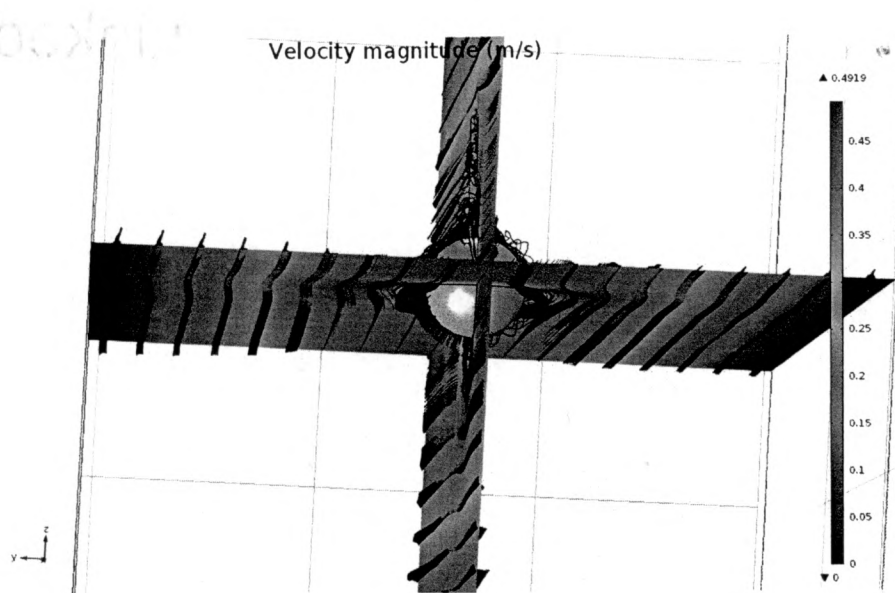Figure 6.2: List of balls and fibers created geometrically using Comsol.

Figure 6.3: The velocity here is governed by two individual slices, one in the xy plane and another in the zx plane. Both of these slices go through the center of the ball. Red signifies high velocity where blue signifies low velocity. The streamlines were only plotted on the individual slices to emphasize the flow around the object. The flow goes into the picture in the x direction.
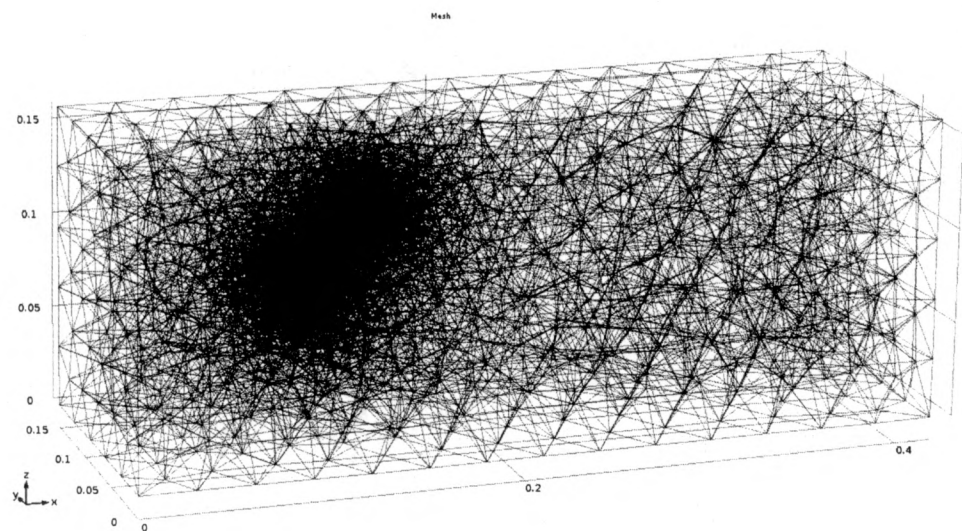

Figure 6.4: The mesh points at which Comsol solves the system of equation. Notice the higher density around the object.